Available online at www.sciencedirect.com

ScienceDirect

Geochimica et Cosmochimica Acta 229 (2018) 85–111

Geochimica et Cosmochimica Acta

www.elsevier.com/locate/gca

Origin of depleted basalts during subduction initiation and early development of the Izu-Bonin-Mariana island arc: Evidence from IODP expedition 351 site U1438, Amami-Sankaku basin

R. Hickey-Vargas [a,*], G.M. Yogodzinski [b], O. Ishizuka [c,d], A. McCarthy [e], M. Bizimis [b], Y. Kusano [c,d], I.P. Savov [f], R. Arculus [g]

[a] *Department of Earth and Environment, AHC5-394, Florida International University, Miami, FL 33199, USA*
[b] *School of Earth, Ocean and Environment, University of South Carolina, 701 Sumter Street, EWSC617, Columbia, SC 29208, USA*
[c] *Geological Survey of Japan/AIST, Central 7 1-1-1 Higashi, Tsukuba, Ibaraki 305-8567, Japan*
[d] *Research and Development Center for Ocean Drilling Science, Japan Agency for Marine-Earth Science and Technology, 2-15 Natsushima-cho, Yokosuka 237-0061, Japan*
[e] *Institute of Earth Sciences, University of Lausanne, Geopolis, Lausanne 1015, Switzerland*
[f] *School of Earth and Environment, University of Leeds, Leeds LS2 9JT, United Kingdom*
[g] *Research School of Earth Sciences, Australian National University, Canberra, ACT 2601, Australia*

Received 28 July 2017; accepted in revised form 4 March 2018; available online 12 March 2018

Abstract

The Izu-Bonin-Mariana (IBM) island arc formed following initiation of subduction of the Pacific plate beneath the Philippine Sea plate at about 52 Ma. Site U1438 of IODP Expedition 351 was drilled to sample the oceanic basement on which the IBM arc was constructed, to better understand magmatism prior to and during the subduction initiation event. Site U1438 igneous basement Unit 1 (150 m) was drilled beneath 1460 m of primarily volcaniclastic sediments and sedimentary rock. Basement basalts are microcrystalline to fine-grained flows and form several distinct subunits (1a-1f), all relatively mafic (MgO = 6.5–13.8%; Mg# = 52–83), with Cr = 71–506 ppm and Ni = 62–342 ppm. All subunits are depleted in non-fluid mobile incompatible trace elements. Ratios such as Sm/Nd (0.35–0.44), Lu/Hf (0.19–0.37), and Zr/Nb (55–106) reach the highest values found in MORB, while La/Yb (0.31–0.92), La/Sm (0.43–0.91) and Nb/La (0.39–0.59) reach the lowest values. Abundances of fluid-mobile incompatible elements, K, Rb, Cs and U, vary with rock physical properties, indicating control by post-eruptive seawater alteration, but lowest abundances are typical of fresh, highly depleted MORBs. Mantle sources for the different subunits define a trend of progressive incompatible element depletion. Inferred pressures of magma segregation are 0.6–2.1 GPa with temperatures of 1280–1470 °C.

New $^{40}Ar/^{39}Ar$ dates for Site U1438 basalts averaging 48.7 Ma (Ishizuka et al., 2018) are younger that the inferred age of IBM subduction initiation based on the oldest ages (52 Ma) of IBM forearc basalts (FAB) from the eastern margin of the Philippine Sea plate. FAB are hypothesized to be the first magma type erupted as the Pacific plate subsided, followed by boninites, and ultimately typical arc magmas over a period of about 10 Ma. Site U1438 basalts and IBM FABs are similar, but Site U1438 basalts have lower V contents, higher Ti/V and little geochemical evidence for involvement of slab-derived fluids. We hypothesize that the asthenospheric upwelling and extension expected during subduction initiation occurred over a broad

* Corresponding author.
E-mail address: hickey@fiu.edu (R. Hickey-Vargas).

https://doi.org/10.1016/j.gca.2018.03.007
0016-7037/

expanse of the upper plate, even as hydrous fluids were introduced near the plate edge to produce FABs and boninites. Site U1438 basalts formed by decompression melting during the first 3 Ma of subduction initiation, and were stranded behind the early IBM arc as mantle conditions shifted to flux melting beneath a well-defined volcanic front.

Keywords: Oceanic basalt; Subduction initiation; Izu-Bonin-Mariana arc; Geochemistry; Ocean drilling

1. INTRODUCTION

The process of subduction is an important influence on the evolution of the Earth's surface and interior features, as well as present day human concerns such as geologic hazards and mineral resources (e.g., McGuire et al., 2017). Despite this, very little is known about how subduction begins. Competing models explain subduction initiation as a spontaneous process, driven by the different densities of juxtaposed lithosphere, or as an induced process where subduction is driven by forces acting laterally on adjacent plates (e.g., Stern, 2004). In 2014, the International Ocean Discovery Program (IODP) sponsored two expeditions, 351 and 352, with the specific goal of understanding the causes and effects of subduction initiation in the Izu-Bonin-Mariana (IBM) island arc system (Fig. 1, Arculus et al., 2015a, 2015b, 2015c; Pearce et al., 2015; Reagan et al., 2015, 2017). Prior research on this system concluded that subduction began at about 52 Ma, nearly simultaneously along its 1000 km length, and was marked by eruption of a specific magma type (Reagan et al., 2010; Ishizuka et al., 2011a). Expedition 351 focused on seafloor hypothesized to be the overriding plate basement upon which the IBM arc was constructed, now located in the back-arc (Fig. 1). Expedition 352 focused on rocks thought to be the earliest magmatic products of IBM subduction initiation, now located in the IBM forearc, close to eastern boundary of the Philippine Sea plate (Fig. 1).

At Site U1438, Expedition 351 drilled 1611 m of sediment, sedimentary and igneous rock in the Amami-Sankaku Basin, just west of the Kyushu Palau Ridge (KPR, Fig. 1). The lithologic sequence here records the formation of the IBM arc basement and the subsequent history of the early IBM arc from arc initiation to arc rifting and back-arc basin formation at about 25 Ma (Arculus et al., 2015a, 2015b, 2015c; Brandl et al., 2017). In this paper, we focus on the geochemical character and origin of the basaltic basement of Site U1438. An important finding is that the basalts have a strongly incompatible trace element-depleted character, similar to the most depleted of mid-ocean ridge basalts (MORB) worldwide, and similar chemically to forearc basalts (FAB) found previously along IBM forearc exposures, the first magmas produced during subduction initiation (Reagan et al., 2010; Ishizuka et al., 2011a). The origin of the Site U1438 basalt sequence, their relationship to IBM forearc FABs, and the differing causes and products of mantle melting during subduction initiation and early IBM development, are explored. In a companion paper (Yogodzinski et al., this volume), Nd, Hf, Sr and Pb isotopes are used to address the origin and age of the depleted mantle sources that were tapped by subduction initiation magmatism and their relationship to global mantle domains and the mantle wedge of the present-day IBM arc.

2. BACKGROUND AND DRILLING SUMMARY

The Amami Sankaku basin Site U1438 was chosen for exploration by Expedition 351 ("Arc Origins") because of its location just west of the KPR, which is an inactive chain of volcanoes forming a remnant arc at the western boundary of the Shikoku and Parece Vela backarc basins (Fig. 1, Karig, 1971; Stern et al., 2001; Ishizuka et al., 2011b). The rocks forming the KPR range in age from about 50 to 25 Ma (Ishizuka et al., 2011b), similar to rocks found in the forearc of the active IBM arc (Fig. 1). It has been inferred that the early IBM arc developed near the KPR on the Philippine Sea plate, with a convergent plate boundary immediately to the east. At about 25 Ma, the early arc rifted, the Shikoku and Parece Vela basins opened through seafloor spreading, and the locus of arc magmatism shifted eastward. Consequently, the distance between the KPR chain of volcanoes and the present-day trench is much greater than originally. The age of the igneous seafloor of the Amami-Sankaku basin was unknown at the time of drilling, but was thought to be as old as Cretaceous based on ages of the adjacent Daito Ridges and Amami Plateau (Fig. 1) (Shiki et al., 1977, Hickey-Vargas, 2005; Ishizuka et al., 2011a).

The drilled section at Site U1438 (Fig. 2) was divided into 4 sedimentary units (Units I, II, II, and IV) which overly igneous basement (Unit 1). Sedimentary Unit I comprises 150 m of Miocene to recent tuffaceous mud and clay with discrete ash layers. Unit II consists of 160 m of late Oligocene tuffaceous mudstone, siltstone and fine sandstone. The underlying Unit III comprises over 1000 m of late Eocene to middle Oligocene tuffaceous sedimentary rocks, ranging from mudstone to breccia-conglomerate. This unit is interpreted to represent the main stage of IBM arc construction to the east of Site U1438 (Arculus et al., 2015a; Brandl et al., 2017). The underlying Unit IV is primarily middle Eocene mudstone, with beds of siltstone, sandstone and breccia, and small (cm-scale) andesitic sills or flows (Arculus et al., 2015b; Ishizuka et al., 2018).

Igneous basement rocks of Unit 1 are microcrystalline to fine grained basalts (Fig. 3), in flows ranging in thickness from a few centimeters to 3–5 m (Ishizuka et al., 2018). Basalts are mainly aphyric and slightly vesicular, with intersertal to diabasic groundmass textures of consisting of clinopyroxene, plagioclase and Fe-Ti oxide minerals. Rare phenocrysts are plagioclase, clinopyroxene and olivine, which is represented mostly by pseudomorphs. Alteration

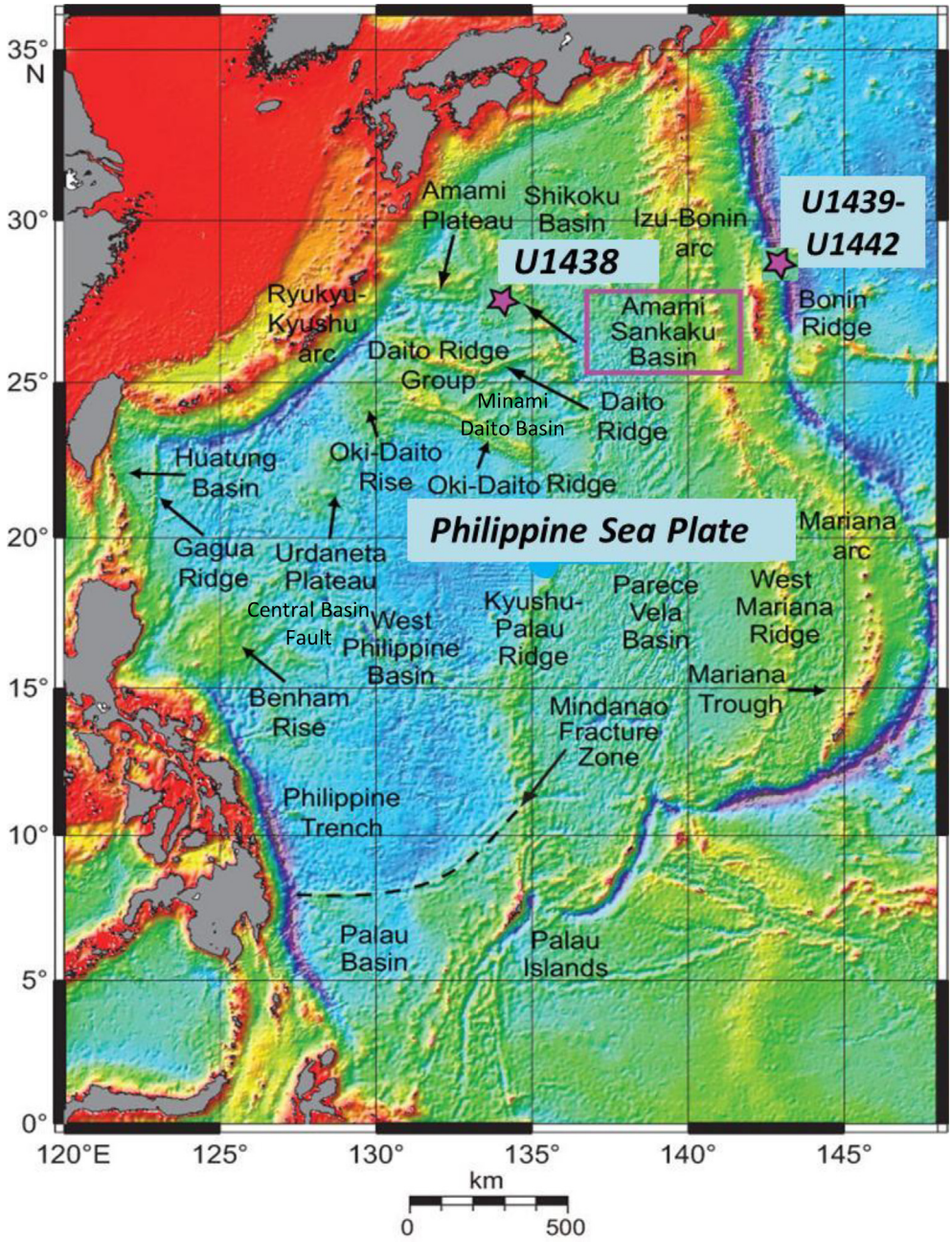

Fig. 1. Map of the Philippine Sea plate showing the location of Expedition 351 Site U1438, Expedition 352 Sites U1439-1442 and surrounding bathymetric features.

is mild to intense on a local basis, but no glass is preserved in the cored section. Olivine is universally altered to chlorite, serpentine and clay, and plagioclase is replaced by zeolites in some areas. Some sections of Unit 1 are cut by fractures and veins, lined with chlorite, quartz, calcite and sulfide minerals.

The most critical information for interpreting Unit 1 in the context of a subduction initiation sequence is the age of the basalts. Based on biostratigraphy and thermal modelling, Arculus et al. (2015b) bracketed the age at 51–64 Ma. These ages were at the young end of ages estimated for the site prior to drilling, and suggested that the basement was formed immediately prior to or contemporaneously with subduction initiation rather than long before it. New $^{40}Ar/^{39}Ar$ ages averaging 48.7 ± 1 Ma have been determined for Unit 1 basalts by Ishizuka et al. (2018). These ages overlap with the range of $^{40}Ar/^{39}Ar$ ages for FABs and overlap with the earliest ages of boninites from the northern and southern parts of the IBM (Reagan et al., 2010; Ishizuka et al., 2011a; Arculus et al., 2015b). However, ages as old as 52 Ma have been obtained for FABs from several forearc locations, and this is the

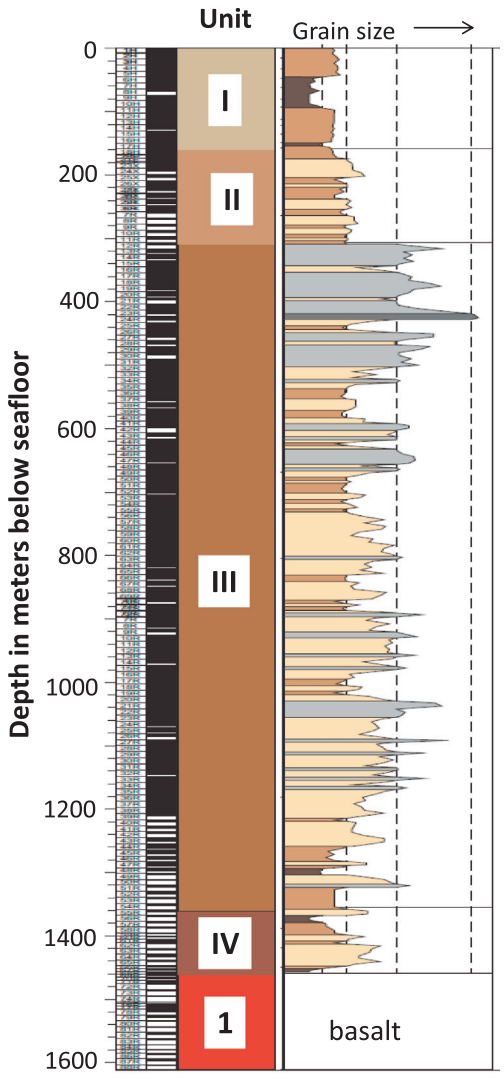

Fig. 2. Schematic diagram of the drilled section at IODP Site U1438, after Arculus et al. (2015a).

presumed age of subduction initiation for the IBM arc (Reagan et al., 2010; Ishizuka et al., 2011a). The younger ages of the Site U1438 basalts indicate that they formed shortly after subduction initiation and at a greater distance from the plate edge than any FABs identified to date. Therefore, understanding their origin, their mantle sources, and their relationship to FABs in the IBM forearc is essential to understanding subduction initiation processes, the incipient IBM arc, and island arc development generally.

3. SAMPLING AND ANALYTICAL METHODS

Ninety-eight basalt samples from Unit 1, together with three samples of andesite sills from Unit IV, were selected for $^{40}Ar/^{39}Ar$ dating, major, trace element and isotopic analysis. For the basement, samples were selected with the goal of including all petrologic types defined by texture and mineralogy and at the same time limiting rocks to those that appeared fresh and relatively free of alteration minerals. These samples were cut and broken into chips, cleaned ultrasonically, then powdered and analyzed for major elements by X-ray fluorescence at the Geological Survey of Japan (GSJ). These data were combined with petrographic observations to select the least altered samples for radioisotope analysis by $^{40}Ar/^{39}Ar$ methods. Major element and $^{40}Ar/^{39}Ar$ dating methods and results are reported in Ishizuka et al. (2018). Aliquots of the same sample powders were distributed to co-authors for trace element and Pb, Sr, Nd and Hf isotopic analysis. Isotopic analytical methods are described by Yogodzinski et al. (this volume). Trace element analytical methods are summarized below.

The Unit 1 and IV samples analyzed for major elements (Ishizuka et al., 2018) were analyzed for trace elements by solution introduction ICP-mass spectrometry at the Trace Evidence Analysis Facility (TEAF) at Florida International University, Miami, USA. Samples (0.05 g) were dissolved with a mixture of high purity HF and HNO_3 (1:2) in sealed savillex beakers, dried down twice with HNO_3 and diluted to 4000 X with distilled deionized water to make a 1.5% HNO_3 solution. Eight rock standards, USGS BIR-1, DNC-1, W-2, BHVO-2, BCR-2, AGV-2 and GSJ JB-2 and JA-2, were dissolved with each of 4 batches of samples, together with a blank. An aliquot of internal standard containing Ge, In and Tm was added to each sample and standard.

Samples were analyzed for: Li, Be, Sc, Rb, Zr, Nb, Cs, Ba, La, Ce, Pr, Nd, Sm, Eu, Tb, Gd, Dy, Ho, Er, Tm, Yb, Lu, Hf, Ta, Pb, Th, and U using a Finnigan Element 2 high resolution sector ICP-MS. Samples were also analyzed for Li, Be, Sc, Ti, V, Cr, Co, Ni, Cu, Zn, Ga, Sr, Y, and other trace elements using a Perkin Elmer Elan DRC-2 quadrupole ICP-MS. In both cases In was used to correct for instrument drift, and the eight standard suite, run at 10–15 sample intervals, was used to correct for mass-related drift if needed. Table 1 lists data for Li, Be, Sc, Ti, V, Cr, Co, Ni, Cu, Zn, Ga, Sr and Y obtained with the Elan and all other elements with the Element 2. Reproducibility for analyses was typically better than 5%, except for Pb and Cs, which were close to their limits of detection in some samples. A table of values obtained for standards, with analytical reproducibility for each element is given in Supplementary Data Table 1.

4. RESULTS

4.1. Down-core changes in major and first transition series trace elements and subunit definition

Major elements and trace elements compatible to moderately incompatible in olivine and pyroxene assemblages show abrupt changes in concentration down-core and provide a basis for defining subunits within the Site U1438 basement section. Six subunits, 1a through 1f were initially defined based on changes in major element concentrations and lithologic features (Ishizuka et al., 2018). In the lower 138 m of the section (subunits 1b-1f), basalts have SiO_2 = 46.4–52.5 wt%, MgO = 6.5–12.1 wt%, Mg# = 52–71 and Na_2O/CaO = 0.1–0.4 (Fig. 4). TiO_2 varies from 0.6 to 1.2%, (Table 1; Fig. 5). Excluding subunit 1a, subunits 1b

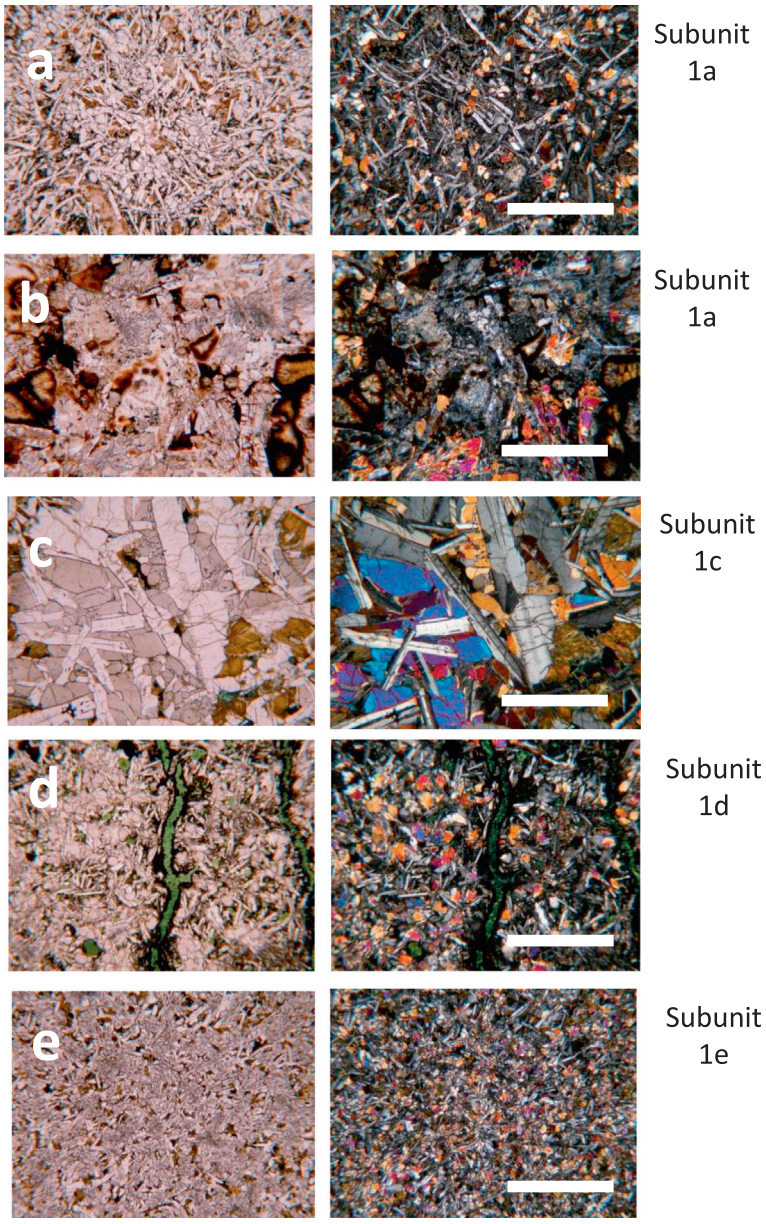

Fig. 3. Petrologic and alteration features of basalts from different subunits of Unit 1 in plane polarized (left) and cross-polarized (right) light. The white bar is 1 mm. (a) Relatively fresh microcrystalline basalt with intersertal texture from subunit 1a (351-U1438E-69-R1 (50–51)); (b) highly altered basalt from subunit 1a, with primary mineral replacement by clay, palagonite and zeolites (351-U1438E-71R-3 (9–10)); (c) Relatively fresh fine-grained basalt from unit 1c, with diabasic to subophitic texture (351-U1438E-79-R1 (18–19)); (d) altered microcrystalline basalt from subunit 1d, with chlorite vein (351-U1438E-83R-1 (111–112)); (e) microcrystalline basalt from subunit 1e (351-U1438E-87R-3 (16–18)).

and 1e have highest Mg# (64–71). Chromium (71–472 ppm), Ni (62–343 ppm), V (177–338 ppm), Sc (36–49 ppm) and Co (43–67 ppm, not shown), show clear breaks at subunit boundaries (Fig. 5; Table 1), with highest Cr in subunits 1b and 1e (276–472). There is a pronounced zone of variable concentrations at the contact between subunits 1c and 1d (1535 mbsf), which is evident in major and incompatible trace elements as well (Figs. 4, 6 and 7).

Subunit 1a is defined as the uppermost 12 m of the section. Here, SiO_2, MgO, Mg# and Na_2O/CaO increase markedly toward the sediment interface and reach values of 57%, 13%, 83.2 and 0.8 respectively. Both total iron as Fe_2O_3 and CaO reach their lowest contents in subunit 1a (Table 1), whereas CaO varies inversely with Fe_2O_3 in other parts of the section. Chromium (305–506 ppm) and Ni contents (82–267 ppm) are similar to those of MgO-rich

Table 1
Trace element concentrations (ppm) in sills in Unit IV and basement basalts from Unit 1, IODP Expedition 351, Site U1438.

(a)

IODP notation	Depth (mbsf)	unit	Li	Be	Sc	Ti	V	Cr	Co	Ni	Cu	Zn	Ga
1438E61R2 3-5	1406.4	IV	24.5	1.42	34.1	4191	251	42	33.4	67	133	124	16.0
1438E61R2 92-95	1407.3	IV	22.8	0.60	36.9	4784	266	45	46.7	79	230	104	15.3
1438E62R1 124-126	1411.6	IV	26.2	0.59	36.3	3972	223	119	48.5	95	290	154	12.8
1438E69R1 44-47	1461.4	1a	11.0	0.34	36.0	2899	126	336	32.8	82	17	54.1	6.5
1438E69R1 98-101	1461.9	1a	46.2	0.25	39.9	3746	165	367	41.7	106	2	57.9	10.5
1438E69R1 134-139	1462.3	1a	38.8	0.16	34.4	3342	125	310	36.5	103	1	52.3	10.3
1438E70R1 5-8	1465.6	1a	51.2	0.19	34.5	3703	194	305	42.9	104	615	78.6	9.7
1438E70R1 54-57	1466.1	1a	42.4	0.18	37.1	3816	214	322	49.0	134	337	54.6	9.8
1438E70R2 16-19	1466.7	1a	39.9	0.31	37.4	4430	177	349	43.2	128	9	70.9	10.4
1438E71R1 33-36	1470.4	1a	73.8	0.15	38.6	3631	182	451	54.4	187	25	66.7	10.9
1438E71R1 98-101	1471.1	1a	44.9	0.16	41.2	4421	245	393	49.3	141	48	73.5	10.3
1438E71R2 5-8	1471.6	1a	35.1	0.12	40.6	4963	221	476	57.6	151	53	90.0	9.1
1438E71R2 84-87	1472.4	1a	19.0	0.15	38.3	4919	208	422	49.7	148	45	90.7	9.5
1438E71R3 10-13	1472.8	1a	58.8	0.18	37.2	4514	223	506	54.2	267	57	64.0	13.4
1438E71R3 101-104	1473.8	1b	27.9	0.21	43.2	4583	222	335	52.7	178	43	63.5	13.4
1438E72R1 76-79	1475.5	1b	8.4	0.13	39.0	4520	206	343	53.2	186	1397	61.7	14.4
1438E72R1 145-148	1476.2	1b	21.4	0.23	45.9	7051	268	307	50.7	95	95	75.7	15.6
1438E73R1 44-47	1484.9	1b	30.8	0.17	38.6	3529	190	327	54.9	226	32	59.7	13.9
1438E73R1 114-117	1485.6	1b	17.3	0.11	38.6	3559	193	367	48.2	194	22	62.6	13.9
1438E73R2 74-77	1486.3	1b	15.6	0.18	39.8	3625	183	356	46.3	186	48	57.6	13.4
1438E73R2 123-128	1486.8	1b	32.0	0.13	38.0	3030	177	472	51.3	255	117	58.5	13.0
1438E74R1 50-55	1494.6	1c	4.2	0.22	43.1	6518	330	127	48.7	65	123	84.6	16.4
1438E74R2 21-24	1495.7	1c	6.8	0.33	48.1	6784	338	166	51.1	80	131	82.8	16.6
1438E75R1 13-17	1504.0	1c	6.2	0.25	41.4	5793	288	193	47.0	100	122	73.3	15.5
1438E75R1 81-85	1504.6	1c	3.4	0.27	43.1	5747	288	269	48.7	91	129	74.5	15.9
1438E76R1 10-15	1506.9	1c	5.2	0.22	42.2	5509	282	265	45.8	84	116	71.4	15.2
1438E76R1 117-122	1508.0	1c	7.0	0.37	48.7	6042	297	297	50.9	95	129	71.7	16.5
1438E76R2 18-21	1508.4	1c	7.4	0.28	42.7	5480	274	224	43.1	80	115	66.0	14.5
1438E76R2 86-91	1509.1	1c	7.1	0.26	42.0	5233	269	265	46.3	87	121	76.9	15.0
1438E76R2 126-130	1509.5	1c	10.3	0.22	42.3	5570	283	268	47.5	88	129	73.6	15.4
1438E76R3 15-18	1509.8	1c	12.9	0.33	47.5	5943	290	287	50.9	97	129	75.8	16.5
1438E76R3 105-110	1510.7	1c	13.0	0.23	38.0	5144	257	227	47.7	106	110	68.2	15.1
1438E77R1 22-25	1511.0	1c	11.2	0.23	40.6	5295	269	253	47.2	98	117	66.5	15.0
1438E77R1 53-58	1511.4	1c	4.7	0.23	42.0	5691	280	257	48.4	100	121	71.9	15.7
1438E77R1 90-95	1511.7	1c	10.5	0.23	40.8	5307	270	268	46.1	100	122	69.3	14.9
1438E77R2 24-27	1512.4	1c	11.1	0.27	40.8	5326	265	276	50.0	119	116	71.1	14.9
1438E77R2 99-101	1513.1	1c	12.6	0.28	44.1	5674	283	348	45.4	78	113	63.8	15.0
1438E77R3 1-4	1513.2	1c	8.2	0.31	44.7	5906	297	340	49.9	88	125	78.8	15.7
1438E77R3 41-43	1513.6	1c	8.0	0.25	43.5	5203	278	262	46.2	87	133	70.1	15.2
1438E78R1 13-18	1515.6	1c	10.8	0.28	43.5	5363	285	203	48.1	78	134	72.4	15.2
1438E78R1 121-124	1516.6	1c	4.0	0.23	44.6	5770	308	215	49.9	81	135	84.4	15.7
1438E78R2 60-65	1517.4	1c	4.6	0.20	42.9	5198	280	224	48.0	86	130	69.8	15.1
1438E78R2 127-130	1518.1	1c	10.1	0.24	47.1	5116	274	281	49.9	96	134	68.2	15.4
1438E78R3 16-21	1518.4	1c	8.2	0.18	38.3	4640	220	241	44.9	89	122	64.4	14.6
1438E78R3 82-85	1519.1	1c	7.4	0.20	41.7	5033	267	231	44.8	89	129	67.0	14.9
1438E78R3 100-103	1519.2	1c	6.7	0.25	42.8	4830	259	268	47.7	92	130	68.3	15.0
1438E78R4 22-25	1519.8	1c	18.5	0.26	40.4	5241	255	305	54.5	165	113	78.8	16.1
1438E78R4 49-53	1520.1	1c	17.8	0.20	36.5	5173	220	250	49.2	141	104	77.7	15.1
1438E79R1 12-17	1524.6	1c	18.1	0.20	40.1	4868	233	292	53.5	173	116	69.4	15.2
1438E79R1 88-91	1525.4	1c	16.0	0.25	39.5	5372	248	265	49.8	146	95	78.8	14.9

(b)

IODP notation	Sr	Y	Zr	Cs	Rb	Ba	Pb	Nb	Ta	Hf	Th	U
1438E61R2 3-5	55.19	14.21	36.5	0.07	2.32	75.0	6.62	0.62	0.05	1.01	0.17	0.47
1438E61R2 92-95	85.83	15.61	41.2	0.09	2.85	187.1	4.32	0.80	0.06	1.35	0.21	0.33
1438E62R1 124-126	93.23	15.14	33.8	0.11	2.88	78.1	2.81	0.56	0.05	0.92	0.15	0.20
1438E69R1 44-47	157.6	17.5	34.8	0.33	11.27	2.3	2.40	0.48	0.038	0.90	0.067	0.211
1438E69R1 98-101	53.8	17.7	37.5	0.28	8.42	1.3	0.35	0.67	0.049	1.09	0.082	0.208
1438E69R1 134-139	101.7	15.2	33.6	0.27	4.27	1.4	0.34	0.60	0.045	0.97	0.075	0.230
1438E70R1 5-8	206.0	13.9	39.3	0.39	13.58	2.5	0.48	0.71	0.054	1.16	0.094	0.150

Table 1 (*continued*)

(b)

IODP notation	Sr	Y	Zr	Cs	Rb	Ba	Pb	Nb	Ta	Hf	Th	U
1438E70R1 54-57	158.2	20.1	40.2	0.10	1.29	7.2	0.32	0.70	0.053	1.13	0.087	0.244
1438E70R2 16-19	291.3	23.5	49.8	0.42	6.00	4.0	0.27	0.87	0.066	1.42	0.109	0.109
1438E71R1 33-36	92.9	16.1	33.7	0.27	10.51	10.7	0.35	0.61	0.049	0.97	0.050	0.048
1438E71R1 98-101	81.2	17.3	37.5	0.18	9.71	7.1	0.33	0.68	0.053	1.17	0.058	0.167
1438E71R2 5-8	221.6	21.4	39.6	0.21	7.93	22.5	0.31	0.56	0.048	1.17	0.043	0.077
1438E71R2 84-87	252.0	20.4	40.0	0.34	10.99	17.6	0.22	0.59	0.049	1.18	0.043	0.124
1438E71R3 10-13	140.2	18.1	37.1	0.26	4.60	3.0	0.21	0.54	0.043	1.15	0.041	0.030
1438E71R3 101-104	142.8	20.3	41.4	0.21	4.52	2.8	0.24	0.45	0.038	1.13	0.033	0.027
1438E72R1 76-79	110.3	21.2	41.3	0.03	0.18	2.3	0.09	0.45	0.037	1.13	0.030	0.010
1438E72R1 145-148	131.1	21.7	38.9	0.13	4.50	9.0	0.26	0.60	0.050	1.18	0.025	0.260
1438E73R1 44-47	113.9	20.2	35.3	0.08	3.41	10.5	0.22	0.42	0.036	0.99	0.031	0.124
1438E73R1 114-117	125.9	20.1	35.2	0.14	5.97	13.3	0.15	0.43	0.037	0.99	0.032	0.059
1438E73R2 74-77	117.8	19.2	35.6	0.10	6.08	15.8	0.68	0.41	0.036	0.99	0.031	0.122
1438E73R2 123-128	71.3	18.4	32.1	0.51	0.70	1.5	0.25	0.39	0.032	0.99	0.031	0.012
1438E74R1 50-55	98.9	28.3	52.4	0.03	0.20	2.5	0.23	0.77	0.062	1.50	0.062	0.023
1438E74R2 21-24	96.1	29.1	51.1	0.08	0.31	3.2	0.61	0.70	0.057	1.40	0.048	0.018
1438E75R1 13-17	89.5	24.3	47.9	0.14	0.23	2.3	0.17	0.73	0.057	1.55	0.052	0.017
1438E75R1 81-85	96.9	26.7	49.0	0.09	0.29	2.3	0.10	0.67	0.055	1.40	0.047	0.018
1438E76R1 10-15	87.2	24.5	44.4	0.28	0.64	2.5	0.23	0.63	0.051	1.29	0.042	0.016
1438E76R1 117-122	95.9	27.1	49.0	0.14	0.48	2.8	0.20	0.66	0.051	1.32	0.048	0.018
1438E76R2 18-21	81.7	22.6	43.9	0.09	0.27	2.5	0.04	0.60	0.047	1.34	0.044	0.017
1438E76R2 86-91	92.2	24.5	45.4	0.13	0.42	2.8	0.38	0.64	0.054	1.35	0.048	0.017
1438E76R2 126-130	89.2	25.4	46.6	0.13	0.43	3.0	0.22	0.65	0.053	1.34	0.044	0.017
1438E76R3 15-18	92.4	26.3	48.2	0.16	0.45	3.1	0.26	0.66	0.052	1.32	0.046	0.018
1438E76R3 105-110	89.9	22.5	42.6	0.17	0.40	2.6	0.17	0.57	0.050	1.22	0.040	0.016
1438E77R1 22-25	88.9	23.6	43.7	0.17	0.41	2.4	0.15	0.61	0.050	1.27	0.042	0.020
1438E77R1 53-58	93.9	24.7	46.2	0.21	0.52	2.4	0.12	0.65	0.053	1.34	0.045	0.017
1438E77R1 90-95	81.6	23.0	45.0	0.20	0.33	2.6	0.13	0.66	0.050	1.47	0.047	0.018
1438E77R2 24-27	87.4	24.1	44.5	0.17	0.52	3.0	0.14	0.64	0.051	1.31	0.046	0.018
1438E77R2 99-101	86.1	24.9	47.0	0.04	0.21	2.8	0.19	0.64	0.053	1.42	0.043	0.037
1438E77R3 1-4	90.7	28.9	49.4	0.03	0.22	3.1	0.26	0.67	0.055	1.46	0.046	0.022
1438E77R3 41-43	85.2	22.0	40.1	0.01	0.01	2.5	0.11	0.55	0.043	1.31	0.040	0.014
1438E78R1 13-18	95.2	23.0	39.9	0.02	0.20	4.0	0.12	0.57	0.050	1.19	0.044	0.016
1438E78R1 121-124	102.8	22.6	40.9	0.02	0.21	3.7	0.13	0.60	0.051	1.22	0.045	0.016
1438E78R2 60-65	96.9	21.5	37.4	0.03	0.21	2.9	0.15	0.54	0.045	1.12	0.041	0.015
1438E78R2 127-130	94.6	22.3	38.3	0.04	0.20	2.9	0.20	0.49	0.039	1.07	0.036	0.014
1438E78R3 16-21	91.5	19.9	35.8	0.03	0.20	2.7	0.11	0.47	0.041	1.07	0.035	0.013
1438E78R3 82-85	85.1	20.5	38.6	0.01	0.03	2.7	0.16	0.52	0.042	1.27	0.039	0.015
1438E78R3 100-103	95.2	21.5	37.4	0.02	0.14	2.9	0.34	0.52	0.067	1.16	0.041	0.015
1438E78R4 22-25	96.2	24.3	42.4	0.03	0.15	2.1	0.35	0.56	0.047	1.24	0.040	0.016
1438E78R4 49-53	86.6	23.9	44.0	0.05	0.24	2.3	0.38	0.59	0.050	1.29	0.042	0.021
1438E79R1 12-17	86.7	22.5	40.0	0.10	0.30	1.7	0.17	0.53	0.043	1.17	0.037	0.016
1438E79R1 88-91	88.4	24.3	44.2	0.03	0.08	2.2	0.10	0.57	0.052	1.28	0.042	0.022

(c)

IODP notation	La	Ce	Pr	Nd	Sm	Eu	Gd	Tb	Dy	Ho	Er	Yb	Lu
1438E61R2 3-5	6.38	16.85	2.29	9.84	2.26	0.81	2.56	0.43	2.47	0.53	1.54	1.49	0.23
1438E61R2 92-95	4.85	14.46	2.31	11.77	2.97	1.07	3.19	0.52	3.30	0.70	2.00	1.94	0.29
1438E62R1 124-126	4.15	11.75	2.05	9.85	2.62	0.91	2.88	0.47	2.70	0.57	1.63	1.59	0.23
1438E69R1 44-47	1.12	3.36	0.63	3.70	1.39	0.53	1.96	0.37	2.49	0.56	1.62	1.62	0.25
1438E69R1 98-101	1.42	4.65	0.82	4.57	1.71	0.63	2.33	0.44	2.98	0.67	1.94	1.94	0.29
1438E69R1 134-139	1.31	4.21	0.73	4.22	1.49	0.57	2.09	0.40	2.67	0.61	1.70	1.74	0.26
1438E70R1 5-8	1.36	4.57	0.77	4.23	1.55	0.55	2.04	0.38	2.44	0.54	1.50	1.49	0.22
1438E70R1 54-57	1.49	4.99	0.87	4.93	1.82	0.66	2.49	0.47	3.25	0.72	2.04	2.12	0.33
1438E70R2 16-19	1.60	5.45	0.94	5.28	1.98	0.64	2.73	0.48	3.53	0.77	2.16	2.02	0.30
1438E71R1 33-36	1.10	3.72	0.66	3.78	1.45	0.54	2.01	0.38	2.63	0.60	1.65	1.64	0.25
1438E71R1 98-101	1.29	4.17	0.78	4.67	1.78	0.65	2.45	0.45	3.15	0.70	1.97	1.92	0.29
1438E71R2 5-8	1.04	3.78	0.73	4.35	1.79	0.62	2.56	0.48	3.53	0.76	2.13	2.15	0.32
1438E71R2 84-87	1.07	3.95	0.74	4.36	1.77	0.64	2.49	0.46	3.35	0.74	2.04	2.01	0.30
1438E71R3 10-13	1.08	3.67	0.71	4.37	1.73	0.67	2.49	0.46	3.26	0.72	2.04	2.04	0.31
1438E71R3 101-104	0.93	3.60	0.69	4.18	1.74	0.69	2.47	0.48	3.34	0.75	2.10	2.09	0.31

(*continued on next page*)

Table 1 (*continued*)

(c)

IODP notation	La	Ce	Pr	Nd	Sm	Eu	Gd	Tb	Dy	Ho	Er	Yb	Lu
1438E72R1 76-79	0.92	3.60	0.70	4.16	1.74	0.68	2.46	0.46	3.38	0.75	2.10	2.15	0.33
1438E72R1 145-148	1.01	3.92	0.76	4.69	2.01	0.80	2.84	0.53	3.71	0.80	2.22	2.12	0.31
1438E73R1 44-47	0.90	3.40	0.65	3.83	1.54	0.62	2.22	0.43	3.14	0.71	2.04	2.12	0.33
1438E73R1 114-117	0.92	3.39	0.63	3.73	1.50	0.61	2.23	0.42	3.12	0.71	2.04	2.05	0.32
1438E73R2 74-77	1.06	3.50	0.66	3.84	1.54	0.62	2.17	0.41	3.03	0.69	1.94	2.07	0.32
1438E73R2 123-128	0.86	3.03	0.61	3.79	1.51	0.64	2.28	0.43	3.20	0.74	2.19	2.30	0.36
1438E74R1 50-55	1.32	5.02	0.94	5.54	2.25	0.81	3.15	0.60	4.47	0.97	2.79	2.86	0.44
1438E74R2 21-24	1.31	5.02	0.94	5.54	2.22	0.84	3.24	0.61	4.46	0.96	2.73	2.83	0.41
1438E75R1 13-17	1.49	5.05	0.96	5.96	2.31	0.89	3.30	0.61	4.50	0.99	2.85	2.89	0.44
1438E75R1 81-85	1.35	4.91	0.91	5.29	2.07	0.76	2.96	0.56	4.13	0.91	2.58	2.69	0.41
1438E76R1 10-15	1.23	4.54	0.82	4.82	1.95	0.72	2.77	0.52	3.89	0.85	2.40	2.43	0.37
1438E76R1 117-122	1.32	4.88	0.89	5.13	2.00	0.78	2.91	0.56	4.01	0.90	2.54	2.57	0.38
1438E76R2 18-21	1.23	4.23	0.82	5.03	2.00	0.77	2.88	0.54	3.87	0.85	2.48	2.49	0.38
1438E76R2 86-91	1.29	4.80	0.87	4.95	1.97	0.76	2.89	0.55	3.98	0.89	2.51	2.62	0.38
1438E76R2 126-130	1.32	4.79	0.87	5.10	1.99	0.74	2.82	0.53	3.98	0.88	2.46	2.53	0.39
1438E76R3 15-18	1.28	4.70	0.88	5.08	1.97	0.77	2.90	0.55	4.00	0.88	2.63	2.64	0.39
1438E76R3 105-110	1.13	4.17	0.78	4.59	1.85	0.69	2.60	0.49	3.62	0.80	2.25	2.33	0.35
1438E77R1 22-25	1.20	4.38	0.80	4.68	1.85	0.69	2.66	0.50	3.72	0.83	2.34	2.39	0.37
1438E77R1 53-58	1.30	4.72	0.86	5.00	1.97	0.73	2.72	0.52	3.84	0.85	2.39	2.48	0.38
1438E77R1 90-95	1.33	4.63	0.89	5.47	2.17	0.83	3.14	0.58	4.21	0.93	2.72	2.77	0.42
1438E77R2 24-27	1.23	4.59	0.86	4.93	1.97	0.73	2.83	0.53	3.96	0.87	2.45	2.51	0.38
1438E77R2 99-101	1.34	4.60	0.86	5.10	2.07	0.73	2.88	0.53	4.07	0.88	2.46	2.53	0.38
1438E77R3 1-4	1.58	5.10	0.95	5.57	2.25	0.80	3.19	0.59	4.46	0.98	2.72	2.77	0.42
1438E77R3 41-43	1.28	4.03	0.80	4.96	2.04	0.80	2.98	0.55	3.97	0.88	2.56	2.51	0.38
1438E78R1 13-18	1.08	3.99	0.75	4.51	1.86	0.70	2.62	0.49	3.64	0.80	2.27	2.34	0.35
1438E78R1 121-124	1.22	4.34	0.79	4.63	1.89	0.72	2.66	0.51	3.70	0.81	2.30	2.49	0.39
1438E78R2 60-65	1.06	3.88	0.72	4.24	1.75	0.66	2.45	0.47	3.42	0.76	2.13	2.17	0.33
1438E78R2 127-130	1.00	3.69	0.68	4.16	1.68	0.69	2.48	0.48	3.37	0.76	2.14	2.17	0.33
1438E78R3 16-21	0.97	3.56	0.67	3.99	1.66	0.64	2.36	0.45	3.26	0.72	2.05	2.10	0.32
1438E78R3 82-85	1.11	3.82	0.76	4.74	1.92	0.77	2.81	0.52	3.76	0.84	2.41	2.43	0.37
1438E78R3 100-103	1.14	4.04	0.75	4.40	1.77	0.71	2.67	0.50	3.64	0.81	2.30	2.37	0.35
1438E78R4 22-25	1.16	4.27	0.76	4.55	1.80	0.71	2.71	0.52	3.75	0.85	2.48	2.46	0.38
1438E78R4 49-53	1.22	4.48	0.82	4.73	1.91	0.71	2.67	0.51	3.77	0.84	2.39	2.50	0.38
1438E79R1 12-17	1.11	4.12	0.76	4.43	1.76	0.70	2.57	0.50	3.65	0.84	2.39	2.44	0.37
1438E79R1 88-91	1.14	4.21	0.79	4.67	1.88	0.71	2.70	0.51	3.84	0.86	2.44	2.55	0.39

(d)

IODP notation	Depth (mbsf)	unit	Li	Be	Sc	Ti	V	Cr	Co	Ni	Cu	Zn	Ga
1438E79R2 6-11	1525.5	1c	18.9	0.20	39.8	5043	247	310	54.8	177	109	75.5	15.4
1438E79R2 57-60	1526.0	1c	15.7	0.21	38.8	5183	223	286	52.6	168	112	70.8	15.3
1438E79R2 106-109	1526.5	1c	18.9	0.32	41.5	5823	282	297	51.9	147	108	80.0	15.4
1438E79R3 26-30	1527.1	1c	13.1	0.31	42.4	5883	294	250	49.4	106	116	80.5	15.9
1438E79R3 87-90	1527.7	1c	17.8	0.33	40.2	5338	267	258	48.7	105	112	75.0	15.7
1438E79R4 0-3	1528.3	1c	12.5	0.26	43.4	6280	304	231	48.1	81	119	79.4	15.9
1438E79R4 48-53	1528.7	1c	15.7	0.32	43.5	6008	281	232	49.0	98	113	75.4	15.9
1438E80R1 17-20	1533.8	1c	8.5	0.27	39.2	5699	296	248	52.8	141	109	74.5	15.0
1438E80R1 60-65	1534.2	1c	21.2	0.29	39.9	5251	267	372	60.1	237	110	75.6	15.5
1438E80R1 90-93	1534.5	1c	19.5	0.24	39.0	5538	275	371	67.1	343	106	77.6	15.0
1438E80R1 131-134	1534.9	1c	35.5	0.29	40.7	5241	277	264	51.0	121	479	81.2	15.5
1438E80R2 27-30	1535.3	1d	11.9	0.25	46.0	5782	294	100	46.7	69	83	83.1	10.3
1438E80R2 35-38	1535.3	1d	10.1	0.24	43.9	5702	305	76	43.6	68	67	72.6	12.5
1438E80R2 49-52	1535.5	1d	15.1	0.27	49.0	6440	337	96	56.2	77	64	83.1	15.8
1438E81R1 25-29	1543.2	1d	5.5	0.22	44.9	5911	291	88	52.6	72	60	74.5	15.2
1438E81R1 114-119	1544.1	1d	7.0	0.26	48.3	6269	308	95	52.7	74	82	82.4	17.1
1438E81R2 32-35	1544.7	1d	6.5	0.21	44.3	5696	290	75	42.9	62	76	70.2	14.6
1438E82R1 6-10	1552.1	1d	6.3	0.23	45.4	6130	295	78	50.2	63	59	77.5	15.3
1438E82R1 61-66	1552.6	1d	7.4	0.21	47.9	5964	292	88	49.0	70	92	79.1	16.2
1438E82R2 28-31	1553.6	1d	7.9	0.22	48.4	6342	304	94	57.8	88	51	84.3	16.6
1438E82R2 102-105	1554.4	1d	7.2	0.24	44.4	5693	284	77	45.7	64	73	69.9	14.4
1438E82R3 12-15	1554.8	1d	6.7	0.25	45.9	5929	306	84	51.8	62	238	76.8	15.0

Table 1 (*continued*)

(d)

IODP notation	Depth (mbsf)	unit	Li	Be	Sc	Ti	V	Cr	Co	Ni	Cu	Zn	Ga
1438E82R3 59-62	1555.3	1d	6.2	0.23	45.9	6117	291	71	51.2	64	59	76.9	15.4
1438E82R3 77-80	1555.5	1d	7.0	0.24	44.5	5471	273	87	51.9	76	72	77.8	15.3
1438E83R1 18-23	1561.6	1d	5.9	0.26	48.3	6071	293	90	47.9	70	54	72.9	14.6
1438E83R1 112-115	1562.5	1d	6.2	0.34	47.4	5911	290	92	49.4	66	68	77.0	16.6
1438E83R1 132-136	1562.7	1d	6.2	0.24	47.1	5969	287	85	49.4	65	132	73.3	14.8
1438E83R2 15-19	1563.0	1d	8.0	0.24	44.6	5720	290	78	45.8	64	83	71.0	14.6
1438E83R2 37-41	1563.2	1d	6.6	0.31	46.9	6191	288	95	51.5	70	56	79.4	16.5
1438E83R2 79-84	1563.6	1d	7.2	0.28	47.7	6197	301	94	48.2	76	59	76.9	14.9
1438E83R3 8-10	1564.3	1d	5.5	0.18	46.3	6023	305	95	52.0	77	46	78.9	14.7
1438E83R3 25-28	1564.5	1d	8.6	0.19	47.0	6024	298	96	54.7	71	91	79.6	16.3
1438E84R1 2-5	1571.1	1d	10.5	0.19	46.1	6011	289	94	52.3	72	83	77.0	14.4
1438E84R1 96-99	1572.1	1e	10.8	0.17	45.2	3914	238	392	48.8	118	74	62.9	13.0
1438E85R1 13-16	1579.2	1e	5.7	0.13	45.0	3862	235	404	57.3	178	19	68.8	12.9
1438E85R1 45-47	1579.6	1e	7.9	0.16	43.6	4085	251	350	47.2	96	190	62.0	12.8
1438E85R1 124-127	1580.4	1e	7.1	0.15	43.5	3910	236	395	52.0	120	144	65.1	13.8
1438E86R1 25-28	1585.2	1e	7.3	0.18	44.6	3929	248	364	49.3	92	148	64.0	13.4
1438E86R1 117-122	1586.1	1e	7.0	0.17	46.6	3980	235	443	56.2	124	144	68.0	13.7
1438E86R2 13-16	1586.4	1e	5.1	0.20	46.1	4051	247	374	47.8	94	117	63.5	14.0
1438E86R2 65-68	1586.9	1e	4.7	0.16	46.9	4027	237	415	65.5	175	147	70.4	13.8
1438E87R1 12-15	1594.1	1e	5.2	0.17	42.4	3817	237	375	52.2	115	144	64.7	13.2
1438E87R1 115-118	1595.2	1e	6.7	0.17	45.7	4367	245	301	50.4	102	152	70.2	13.7
1438E87R1 132-135	1595.3	1e	8.0	0.16	45.3	4311	253	346	45.7	100	137	61.9	13.3
1438E87R2 0-3	1595.4	1e	7.1	0.17	46.9	4109	243	330	50.4	99	149	67.5	13.8
1438E87R2 33-36	1595.8	1e	8.0	0.20	45.1	4439	260	290	53.4	101	155	76.9	14.8
1438E87R3 13-16	1596.0	1e	7.5	0.20	46.6	4456	262	277	50.1	92	160	71.3	14.5
1438E87R3 56-60	1596.4	1e	6.9	0.16	47.2	3887	237	430	48.1	112	139	63.8	13.7
1438E87R3 108-112	1596.9	1e	7.4	0.19	44.8	4197	261	361	50.5	102	151	69.0	14.8
1438E88R1 98-101	1604.1	1f	8.3	0.17	45.1	4938	272	152	44.0	85	68	65.0	14.0
1438E88R1 142-145	1604.5	1f	8.3	0.23	45.2	4766	258	194	55.3	105	30	73.5	14.4

(e)

IODP notation	Sr	Y	Zr	Cs	Rb	Ba	Pb	Nb	Ta	Hf	Th	U
1438E79R2 6-11	91.3	23.9	42.4	0.05	0.19	1.9	0.28	0.55	0.046	1.25	0.043	0.020
1438E79R2 57-60	89.7	23.0	40.8	0.02	0.08	2.1	0.19	0.52	0.047	1.22	0.038	0.017
1438E79R2 106-109	91.0	17.6	47.7	0.01	0.29	3.3	0.49	0.67	0.051	1.51	0.049	0.033
1438E79R3 26-30	94.0	26.8	49.7	0.01	0.05	2.7	0.15	0.63	0.055	1.48	0.046	0.019
1438E79R3 87-90	91.7	25.9	47.8	0.02	0.13	3.0	0.22	0.66	0.053	1.41	0.048	0.019
1438E79R4 0-3	89.7	26.3	51.9	0.01	0.05	2.8	0.12	0.66	0.059	1.52	0.044	0.026
1438E79R4 48-53	82.7	26.6	49.8	0.06	0.22	2.8	0.23	0.68	0.054	1.46	0.046	0.018
1438E80R1 17-20	90.8	25.7	49.6	0.04	2.27	3.3	0.21	0.62	0.053	1.40	0.045	0.096
1438E80R1 60-65	85.1	24.0	44.5	0.03	0.15	2.3	0.09	0.60	0.050	1.38	0.047	0.017
1438E80R1 90-93	79.6	24.1	43.5	0.02	0.08	2.2	0.06	0.57	0.051	1.31	0.044	0.017
1438E80R1 131-134	85.7	24.3	46.0	0.09	3.66	9.0	0.48	0.60	0.049	1.40	0.048	0.068
1438E80R2 27-30	197.4	23.3	32.5	0.30	16.70	81.4	0.64	0.56	0.046	0.96	0.030	0.563
1438E80R2 35-38	158.8	20.9	32.1	0.15	9.41	106.5	0.36	0.54	0.045	1.03	0.031	0.215
1438E80R2 49-52	72.0	25.6	45.4	0.14	13.48	5.2	0.28	0.62	0.056	1.44	0.044	0.201
1438E81R1 25-29	95.6	22.5	39.7	0.09	8.57	7.7	0.17	0.54	0.051	1.24	0.039	0.134
1438E81R1 114-119	106.3	25.0	43.1	0.16	12.97	7.1	0.18	0.58	0.046	1.24	0.040	0.085
1438E81R2 32-35	84.4	20.7	39.9	0.11	9.11	5.8	0.15	0.53	0.045	1.25	0.037	0.078
1438E82R1 6-10	95.8	23.3	42.0	0.12	8.48	6.4	0.20	0.56	0.053	1.31	0.040	0.120
1438E82R1 61-66	95.5	23.6	41.6	0.19	10.76	6.4	0.23	0.58	0.050	1.23	0.040	0.078
1438E82R2 28-31	106.1	25.5	44.3	0.05	5.46	8.3	0.22	0.58	0.046	1.25	0.042	0.241
1438E82R2 102-105	84.0	20.8	39.3	0.13	8.21	5.7	0.09	0.51	0.042	1.24	0.036	0.101
1438E82R3 12-15	95.4	21.7	40.5	0.10	7.26	6.1	0.27	0.55	0.048	1.27	0.038	0.131
1438E82R3 59-62	93.4	23.0	39.4	0.15	11.90	9.0	0.18	0.53	0.052	1.30	0.040	0.178
1438E82R3 77-80	96.2	22.6	39.4	0.08	6.99	6.3	0.17	0.55	0.047	1.25	0.041	0.153
1438E83R1 18-23	92.3	20.6	39.2	0.12	10.44	9.0	0.17	0.53	0.049	1.24	0.038	0.097
1438E83R1 112-115	92.6	22.2	41.0	0.20	18.80	11.7	0.47	0.57	0.047	1.20	0.039	0.070
1438E83R1 132-136	92.7	21.9	39.0	0.11	8.30	6.9	0.20	0.53	0.048	1.25	0.037	0.114
1438E83R2 15-19	84.2	20.5	39.6	0.12	8.10	5.9	0.06	0.52	0.039	1.15	0.035	0.083
1438E83R2 37-41	101.8	24.0	40.8	0.15	13.53	9.0	0.21	0.58	0.053	1.25	0.042	0.221
1438E83R2 79-84	94.3	21.6	40.7	0.09	8.41	6.7	0.19	0.56	0.063	1.31	0.039	0.110

(*continued on next page*)

Table 1 (*continued*)

(e)

IODP notation	Sr	Y	Zr	Cs	Rb	Ba	Pb	Nb	Ta	Hf	Th	U
1438E83R3 8-10	94.6	22.1	41.0	0.03	5.70	13.7	0.15	0.54	0.049	1.28	0.039	0.068
1438E83R3 25-28	100.5	23.2	41.5	0.08	7.75	9.1	0.19	0.55	0.048	1.26	0.041	0.057
1438E84R1 2-5	135.9	23.7	41.4	0.15	11.99	28.6	0.25	0.57	0.048	1.28	0.042	0.110
1438E84R1 96-99	148.0	17.1	26.3	0.15	10.34	54.6	0.29	0.30	0.028	0.87	0.020	0.100
1438E85R1 13-16	136.5	17.5	27.8	0.05	7.12	30.3	0.18	0.28	0.029	0.90	0.019	0.041
1438E85R1 45-47	88.7	16.3	27.8	0.05	5.44	19.1	0.08	0.26	0.024	0.87	0.018	0.070
1438E85R1 124-127	80.0	16.5	26.8	0.01	0.08	1.9	0.20	0.30	0.027	0.88	0.020	0.011
1438E86R1 25-28	110.7	17.3	26.8	0.15	8.41	26.2	0.28	0.30	0.027	0.86	0.022	0.117
1438E86R1 117-122	84.5	16.3	28.6	0.00	0.31	4.2	0.35	0.29	0.030	0.93	0.020	0.011
1438E86R2 13-16	75.1	17.7	27.3	0.13	7.88	7.3	0.19	0.31	0.028	0.86	0.020	0.052
1438E86R2 65-68	79.0	17.1	28.9	0.00	0.32	2.7	0.14	0.31	0.030	0.95	0.022	0.102
1438E87R1 12-15	74.3	16.0	26.9	0.01	0.14	2.4	0.28	0.31	0.028	0.88	0.021	0.008
1438E87R1 115-118	74.7	18.8	29.8	0.01	1.26	2.5	0.30	0.31	0.033	0.98	0.022	0.033
1438E87R1 132-135	68.9	15.6	29.1	0.00	0.01	1.5	0.19	0.28	0.024	0.93	0.020	0.011
1438E87R2 0-3	74.7	17.5	29.7	0.00	0.03	2.1	0.13	0.30	0.031	0.97	0.021	0.011
1438E87R2 33-36	77.5	17.7	30.4	0.01	0.06	2.1	0.26	0.34	0.030	0.99	0.024	0.009
1438E87R3 13-16	71.4	19.0	30.4	0.02	0.14	1.6	0.16	0.35	0.031	0.97	0.024	0.008
1438E87R3 56-60	73.6	17.3	27.5	0.01	0.14	1.5	0.11	0.29	0.028	0.87	0.020	0.008
1438E87R3 108-112	74.4	18.4	28.3	0.01	0.06	2.1	0.06	0.31	0.030	0.94	0.023	0.007
1438E88R1 98-101	79.1	20.4	37.2	0.09	6.50	8.7	0.07	0.38	0.033	1.15	0.028	0.095
1438E88R1 142-145	90.0	20.5	37.6	0.02	1.76	8.5	0.17	0.41	0.037	1.18	0.034	0.055

(f)

IODP notation	La	Ce	Pr	Nd	Sm	Eu	Gd	Tb	Dy	Ho	Er	Yb	Lu
1438E79R2 6-11	1.17	4.27	0.79	4.60	1.84	0.70	2.67	0.52	3.78	0.86	2.46	2.54	0.38
1438E79R2 57-60	1.15	4.10	0.77	4.52	1.80	0.70	2.61	0.49	3.68	0.82	2.33	2.42	0.37
1438E79R2 106-109	1.72	4.33	0.92	5.32	1.90	0.80	2.65	0.48	3.38	0.73	2.10	2.17	0.33
1438E79R3 26-30	1.45	4.97	0.92	5.32	2.10	0.77	3.00	0.56	4.27	0.95	2.77	2.89	0.44
1438E79R3 87-90	1.38	5.19	0.95	5.43	2.18	0.82	3.10	0.59	4.30	0.95	2.70	2.73	0.41
1438E79R4 0-3	1.42	5.26	0.97	5.71	2.23	0.82	3.07	0.58	4.32	0.94	2.67	2.73	0.42
1438E79R4 48-53	1.39	5.25	0.99	5.68	2.22	0.83	3.20	0.61	4.44	0.97	2.81	2.83	0.42
1438E80R1 17-20	1.36	4.96	0.90	5.23	2.05	0.76	2.92	0.55	4.14	0.91	2.58	2.65	0.41
1438E80R1 60-65	1.28	4.75	0.88	5.15	1.98	0.75	2.87	0.54	3.96	0.90	2.56	2.52	0.39
1438E80R1 90-93	1.23	4.61	0.86	5.05	2.02	0.72	2.83	0.53	3.94	0.87	2.45	2.55	0.39
1438E80R1 131-134	1.41	4.99	0.90	5.13	2.02	0.77	2.96	0.55	4.14	0.91	2.61	2.57	0.40
1438E80R2 27-30	1.20	4.24	0.78	4.56	1.88	0.76	2.80	0.53	3.80	0.84	2.39	2.33	0.35
1438E80R2 35-38	1.10	3.82	0.76	4.74	1.90	0.79	2.78	0.51	3.67	0.81	2.30	2.22	0.34
1438E80R2 49-52	1.27	4.62	0.85	5.08	2.08	0.78	3.00	0.56	4.28	0.93	2.68	2.72	0.42
1438E81R1 25-29	1.05	3.86	0.77	4.62	1.91	0.73	2.69	0.51	3.79	0.83	2.34	2.42	0.37
1438E81R1 114-119	1.13	4.16	0.78	4.63	1.87	0.75	2.73	0.52	3.79	0.85	2.41	2.41	0.37
1438E81R2 32-35	1.09	3.76	0.74	4.63	1.89	0.75	2.75	0.51	3.77	0.82	2.36	2.35	0.36
1438E82R1 6-10	1.17	4.25	0.82	4.86	2.01	0.76	2.80	0.53	3.89	0.85	2.38	2.47	0.37
1438E82R1 61-66	1.15	4.27	0.79	4.59	1.91	0.75	2.81	0.53	3.86	0.86	2.43	2.46	0.36
1438E82R2 28-31	1.15	4.28	0.80	4.80	1.92	0.78	2.84	0.53	3.97	0.86	2.46	2.50	0.38
1438E82R2 102-105	1.01	3.61	0.73	4.57	1.87	0.75	2.70	0.50	3.62	0.80	2.28	2.28	0.34
1438E82R3 12-15	1.01	3.84	0.72	4.33	1.83	0.71	2.60	0.49	3.67	0.80	2.28	2.35	0.35
1438E82R3 59-62	1.07	4.06	0.81	4.89	2.03	0.77	2.85	0.54	4.02	0.88	2.45	2.55	0.39
1438E82R3 77-80	1.08	4.00	0.77	4.63	1.83	0.75	2.77	0.53	3.76	0.82	2.30	2.39	0.36
1438E83R1 18-23	1.04	3.86	0.75	4.47	1.86	0.72	2.59	0.49	3.56	0.78	2.16	2.25	0.34
1438E83R1 112-115	1.05	4.07	0.74	4.47	1.85	0.74	2.72	0.51	3.70	0.82	2.35	2.36	0.35
1438E83R1 132-136	1.12	4.07	0.77	4.58	1.88	0.72	2.64	0.50	3.69	0.80	2.26	2.30	0.35
1438E83R2 15-19	1.00	3.44	0.70	4.45	1.85	0.75	2.72	0.51	3.64	0.80	2.30	2.21	0.33
1438E83R2 37-41	1.11	4.11	0.78	4.70	1.97	0.76	2.82	0.54	3.92	0.86	2.40	2.41	0.37
1438E83R2 79-84	1.09	4.11	0.79	4.67	1.93	0.75	2.70	0.51	3.81	0.84	2.36	2.42	0.37
1438E83R3 8-10	1.05	3.96	0.77	4.61	1.93	0.74	2.71	0.51	3.81	0.83	2.31	2.37	0.36
1438E83R3 25-28	1.10	4.10	0.77	4.61	1.88	0.75	2.75	0.53	3.81	0.84	2.36	2.36	0.36
1438E84R1 2-5	1.18	4.21	0.80	4.75	1.93	0.76	2.82	0.54	3.89	0.88	2.46	2.47	0.38
1438E84R1 96-99	0.66	2.60	0.52	3.22	1.40	0.60	2.05	0.42	2.93	0.66	1.85	1.91	0.29
1438E85R1 13-16	0.63	2.46	0.51	3.20	1.40	0.59	2.09	0.40	2.93	0.66	1.87	1.94	0.29
1438E85R1 45-47	0.63	2.34	0.49	3.17	1.35	0.58	2.03	0.39	2.77	0.63	1.79	1.82	0.27

Table 1 (*continued*)

(f)

IODP notation	La	Ce	Pr	Nd	Sm	Eu	Gd	Tb	Dy	Ho	Er	Yb	Lu
1438E85R1 124-127	0.64	2.55	0.50	3.15	1.36	0.57	2.03	0.40	2.88	0.64	1.84	1.87	0.29
1438E86R1 25-28	0.70	2.72	0.54	3.29	1.40	0.58	2.08	0.41	2.91	0.66	1.89	1.92	0.30
1438E86R1 117-122	0.62	2.48	0.52	3.23	1.40	0.58	2.06	0.40	2.93	0.65	1.83	1.94	0.30
1438E86R2 13-16	0.67	2.67	0.52	3.31	1.38	0.58	2.09	0.41	2.87	0.67	1.92	1.96	0.29
1438E86R2 65-68	0.65	2.69	0.54	3.33	1.43	0.58	2.08	0.40	2.95	0.66	1.87	1.92	0.29
1438E87R1 12-15	0.63	2.55	0.52	3.09	1.34	0.57	2.04	0.40	2.80	0.64	1.82	1.83	0.28
1438E87R1 115-118	0.66	2.74	0.56	3.50	1.53	0.62	2.21	0.43	3.20	0.71	2.03	2.16	0.33
1438E87R1 132-135	0.58	2.27	0.48	3.17	1.35	0.57	2.03	0.39	2.75	0.61	1.75	1.76	0.26
1438E87R2 0-3	0.62	2.60	0.54	3.38	1.46	0.59	2.13	0.41	3.02	0.67	1.88	1.96	0.30
1438E87R2 33-36	0.71	2.98	0.58	3.53	1.47	0.61	2.17	0.43	3.04	0.68	1.93	2.03	0.32
1438E87R3 13-16	0.69	2.98	0.58	3.65	1.58	0.63	2.26	0.45	3.20	0.73	2.09	2.13	0.33
1438E87R3 56-60	0.61	2.51	0.51	3.16	1.37	0.52	2.05	0.41	2.86	0.64	1.79	1.85	0.29
1438E87R3 108-112	0.70	2.85	0.56	3.50	1.47	0.61	2.21	0.43	3.09	0.70	1.98	2.03	0.31
1438E88R1 98-101	0.90	3.23	0.66	4.20	1.75	0.70	2.60	0.49	3.55	0.79	2.33	2.36	0.36
1438E88R1 142-145	0.88	3.45	0.68	4.06	1.76	0.70	2.52	0.50	3.61	0.80	2.29	2.30	0.35

subunit 1b and 1e basalts, while V (125–245 ppm), Sc (34.4–41.2 ppm) and Ti (2900–4960 ppm) contents are lower (Fig. 5). Loss on ignition (LOI) is generally 1–5% in subunits 1b-1f, but ranges from 5–11% in subunit 1a (Ishizuka et al., 2018).

4.2. Down-core changes in incompatible trace element abundances and ratios

Elements commonly mobilized by aqueous fluids, through processes such as post-eruptive hydrothermal alteration or dehydration of the subducted oceanic crust, show several distinct variations in the section. Like MgO and SiO_2, Na_2O and Sr concentrations are highest at the top of the section in subunit 1a (Figs. 4 and 6). In contrast, K, Rb and U abundances (Fig. 6), together with Cs (Table 1), increase and decrease concomitantly down-core in correspondence with the subunits defined by other major and trace elements. The lowest abundances of these elements are found in subunits 1c and the lower part of 1e, with high and variable abundances in subunits 1a, 1b, 1d the upper part of 1e. Ba, Pb, Cu and Zn concentrations also vary somewhat with subunit boundaries, but have a more random distribution in the section (Table 1).

Abundances and ratios of high field strength elements (HFSE) Th, Nb, Ta, Hf, Zr, and rare earth elements (REE) correlate with subunits defined by major and compatible elements. Subunit 1e has the lowest HFSE and REE abundances (Fig. 8; Table 1). Ratios of trace elements with differing incompatibility, such as Ti/V, Zr/Nb, La/Yb, and Lu/Hf (Fig. 7a and b), vary widely in subunits 1a and 1b and at the interface of subunits 1c and 1d. In contrast, these ratios are relatively constant within subunits 1c, 1d and 1e, with highly incompatible elements most depleted (i.e., high Zr/Nb and Lu/Hf, and low Ti/V and La/Yb) in subunit 1e (Fig. 7a and b). Ratios of elements with similar incompatibility, such as Sm/Nd, Hf/Sm, La/Nb and Th/Nb, also vary most within subunits 1a and 1b, and at the contact of subunits 1c and 1d. These ratios are relatively constant within subunits 1c, 1d and 1e, with higher Sm/Nd in subunit 1e, but no systematic change down-core in Th/Nb, La/Nb and Hf/Sm. In subunit 1a, Th, La and Nd abundances increase upward toward the sediment/basalt contact (Fig. 11), resulting in highest La/Yb and Th/Nb, and lowest Sm/Nd (Fig. 7a and b).

4.3. Normalized incompatible element trace element patterns

Fig. 8a and b shows primitive mantle normalized abundances of fluid immobile trace elements and REE in subunits 1c and 1e of Unit 1, compared with MORB and FAB. All Site U1438 basalts have exceptionally low abundances of highly incompatible immobile trace elements, 0.4–1.2 times primitive mantle in subunits 1c and 1e, which is lower than N-MORB and D-MORB averages from different studies (Fig. 8). Slightly incompatible elements such as the heavy rare earth elements (HREE) reach normalized concentrations of 3–6 times primitive mantle, and these are also lower than MORB averages. REE patterns have normalized $(La/Sm)_N$ of 0.28 to 0.57 and $(La/Yb)_N$ of 0.22 to 0.66, with relatively flat HREE abundances. HREE abundances in Site U1438 basalts and FABs overlap (Fig. 8b) but abundances of Th, Nb, Ta and La are higher in FABs than the most depleted Unit 1 basalts.

Fluid mobile elements, normalized to N-MORB (Fig. 9), show prominent and variable enrichment of Cs (not shown), Rb, Ba, U, K, Pb and Sr compared with the fluid-immobile elements. However, subunits 1b, 1c and 1e each include some basalts having normalized concentrations of these elements like those of adjacent immobile elements (Fig. 9), and thus similar to MORB.

In summary, Site U1438 Unit 1 basalts are more depleted in immobile incompatible elements and highly/moderately incompatible element ratios than published N-MORB and D-MORB averages (Fig. 8). Highly incompatible fluid-mobile elements exhibit wide variations associated with specific subunits, and reach similar MORB-like low abundances in subunits 1b, 1c and the lower part of

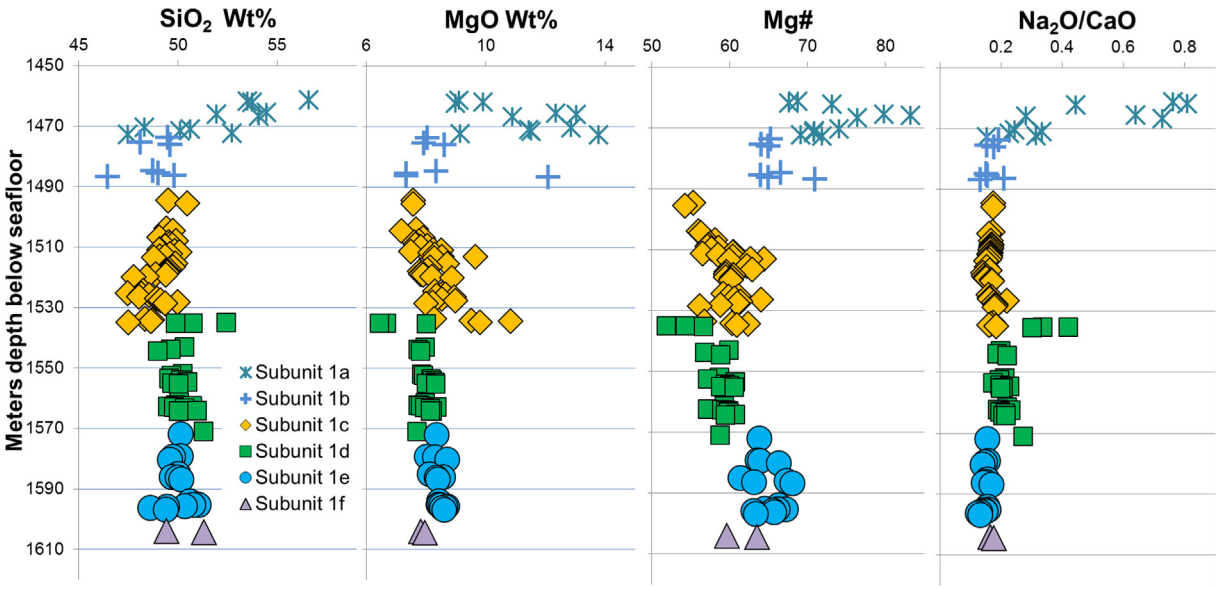

Fig. 4. Down-core variation of select major element data for basement Unit 1, showing boundaries for subunits 1a through 1f. Data are from Ishizuka et al. (2018).

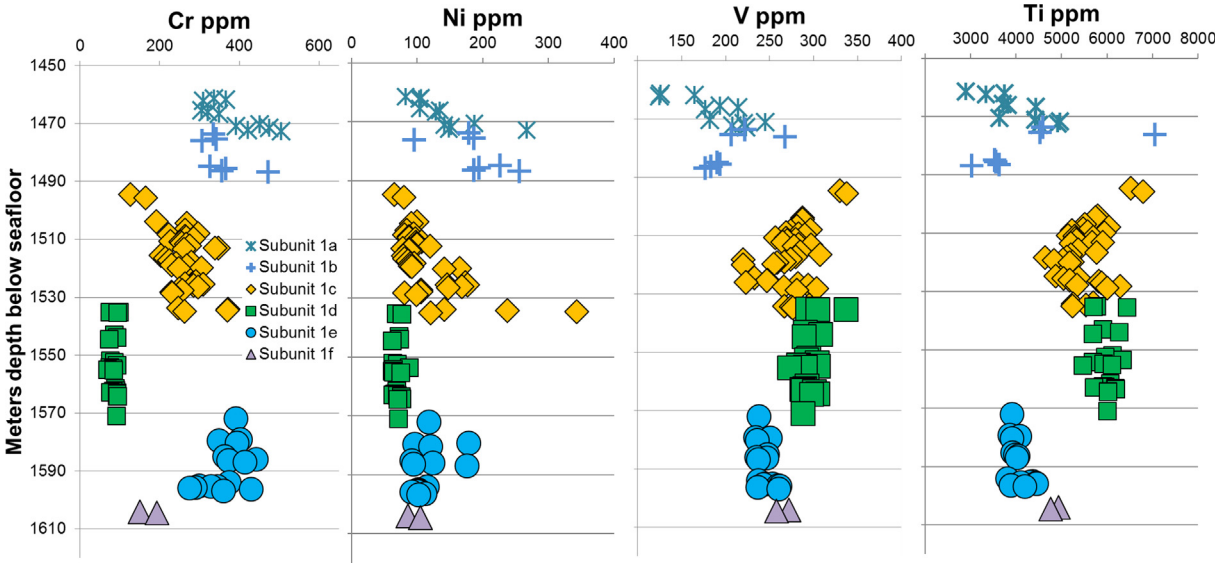

Fig. 5. Down-core variation of Cr, Ni, V and Ti abundances with subunit boundaries. Data are from Table 1.

1e (Fig. 9). Subunit 1a is enriched in fluid mobile elements and shows slight enrichments in Th, Nb, Ta, La and Nd, although still more depleted than MORB (Fig. 11).

4.4. Basaltic andesites of Unit IV

Volcanic rock was encountered within sedimentary Unit IV in the interval 1396–1412 m below seafloor (Fig. 2). These rocks have been interpreted as sills or as "invasive" flows that submerged into soft sediment (Arculus et al., 2015b, 2015c; Ishizuka et al., 2018). The rocks exhibit chilled margins and surrounding sediments are deformed. Radiometric ages have not been obtained, however microfossils indicate an age of 42 ± 3 for this part of Unit IV (Arculus et al., 2015c). Three samples are medium K basalt andesite (54.7% SiO_2, K_2O 0.3–0.6%) with TiO_2 0.7–0.8% (Ishizuka et al., 2018). Like uppermost basement subunit 1a, MgO contents, LOI and Na_2O/CaO in these rocks are high (8.6–9.1%, 4.6–5.1% and 0.9–1.5 respectively). Normalized trace element abundances (Fig. 8c) have the characteristic features of island arc magmas; fluid mobile incompatible trace elements Rb, Ba, U and Pb are enriched relative to REE, and HFSE are depleted, with normalized $(La/Nb)_N = 6.9–10.6$ and $(Sm/Hf)_N = 1.5–2.0$. LREE are

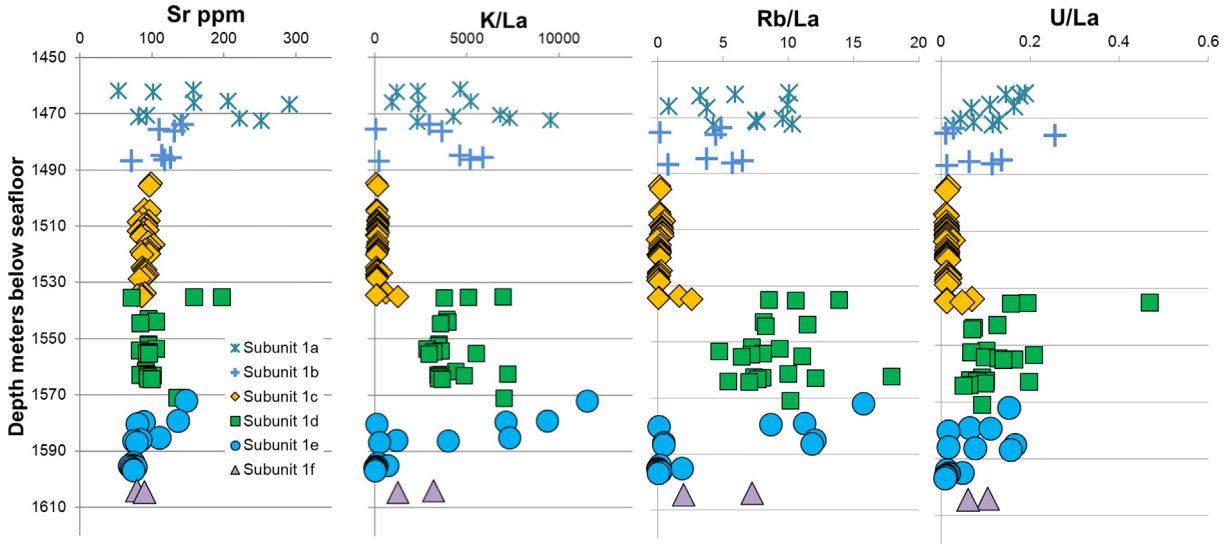

Fig. 6. Down-core variation of Sr abundances and K, Rb, and U abundances relative to La showing correspondence with subunit boundaries. Data are from Table 1.

enriched compared to HREE (normalized $(La/Yb)_N = 1.7–3.1$) and HREE abundances are slightly lower than those of the Unit 1 basalts (Fig. 8c).

5. DISCUSSION

Prior to drilling, the basaltic section at Site U1438 was inferred to be the pre-existing oceanic lithosphere on which the IBM arc was built, possibly as old as Cretaceous based on the age of surrounding remnant arcs, the Daito Ridge and Amami Plateau (Shiki et al., 1977; Hickey-Vargas, 2005; Ishizuka et al., 2011b). The inference that it represented oceanic basement was based on the location of the Amami-Sankaku basin to the west of the KPR remnant arc, presumed to be the initial locus of IBM arc volcanism, and the relatively flat, undeformed and thickly sedimented nature of the basin floor (Taylor et al., 1992; Higuchi et al., 2007). The young age of the basalts, inferred first through biostratigraphy, sedimentological, geophysical means (Arculus et al., 2015b), and then determined through $^{40}Ar/^{39}Ar$ dating (Ishizuka et al., 2018) indicates that Site U1438 basalts may have formed as much as 3 Ma after subduction initiation, as inferred from the age of the oldest IBM FABs. At 48.7 Ma, the location of Site U1438 was proximal to the northern Pacific/Philippine plate margin where FABs have yielded $^{40}Ar/^{39}Ar$ ages of 52–48 Ma (Ishizuka et al., 2011a, 2018). Recent findings of IODP Expedition 352 in the same area reveal that FABs were erupted before boninites and closer to the trench (Reagan et al., 2017). Since Site U1438 basalts were erupted within the earliest 3 Ma of subduction initiation in a region close to, but further from the plate edge than boninites, they provide new information about the extent and conditions of mantle melting and magma generation during arc inception. In this discussion, we: (1) consider the origin of the geochemical subunits and identify geochemical features of the basalts which are primary igneous features; (2) compare the primary features of Site U1438 basalts to those of FAB recovered from the IBM forearc and MORB to identify possible relationships; and (3) consider the melting and arc-evolution processes that produced the magmas erupted at Site U1438 together with boninite and FAB in the forearc.

5.1. Geochemical subunits and their significance

The subunit division of the Site U1438 section was initially based on changes in the major element composition of basalts supported by lithologic analysis of the cored section, including the location of flow boundaries and chilled margins, changes in rock texture, and apparent short hiatuses indicated by interbedded sediment (Ishizuka et al., 2018).

Based on the correlation of major and compatible element trends, our interpretation is that geochemical subunits formed from distinct batches of basaltic magma, which were each erupted on the seafloor as multiple lava flows of varying thickness. Subunit 1c (1495–1535 mbsf) consists of massive, 2–5 m thick lava flows with fine-grained texture (Fig. 3c), whereas most other subunits are composed of multiple thinner lava flows with microcrystalline texture (Fig. 3a and e). Although there are down-core geochemical differences between magma batches, there is little evidence for magmatic differentiation by crystallization over the course of subunit eruption. Major and compatible trace element contents are not well correlated within subunits, although there is weak overall covariation of Cr and Mg# for the whole basement sequence (Fig. 10a). Since the basalts have Mg#, Ni and Cr contents too low for primary magmas in equilibrium with mantle peridotite, our interpretation is that primary melts forming each subunit aggregated and differentiated at depth, and then rose and erupted as lavas flows on the ocean floor in short episodes, such that further differentiation was not notable. This

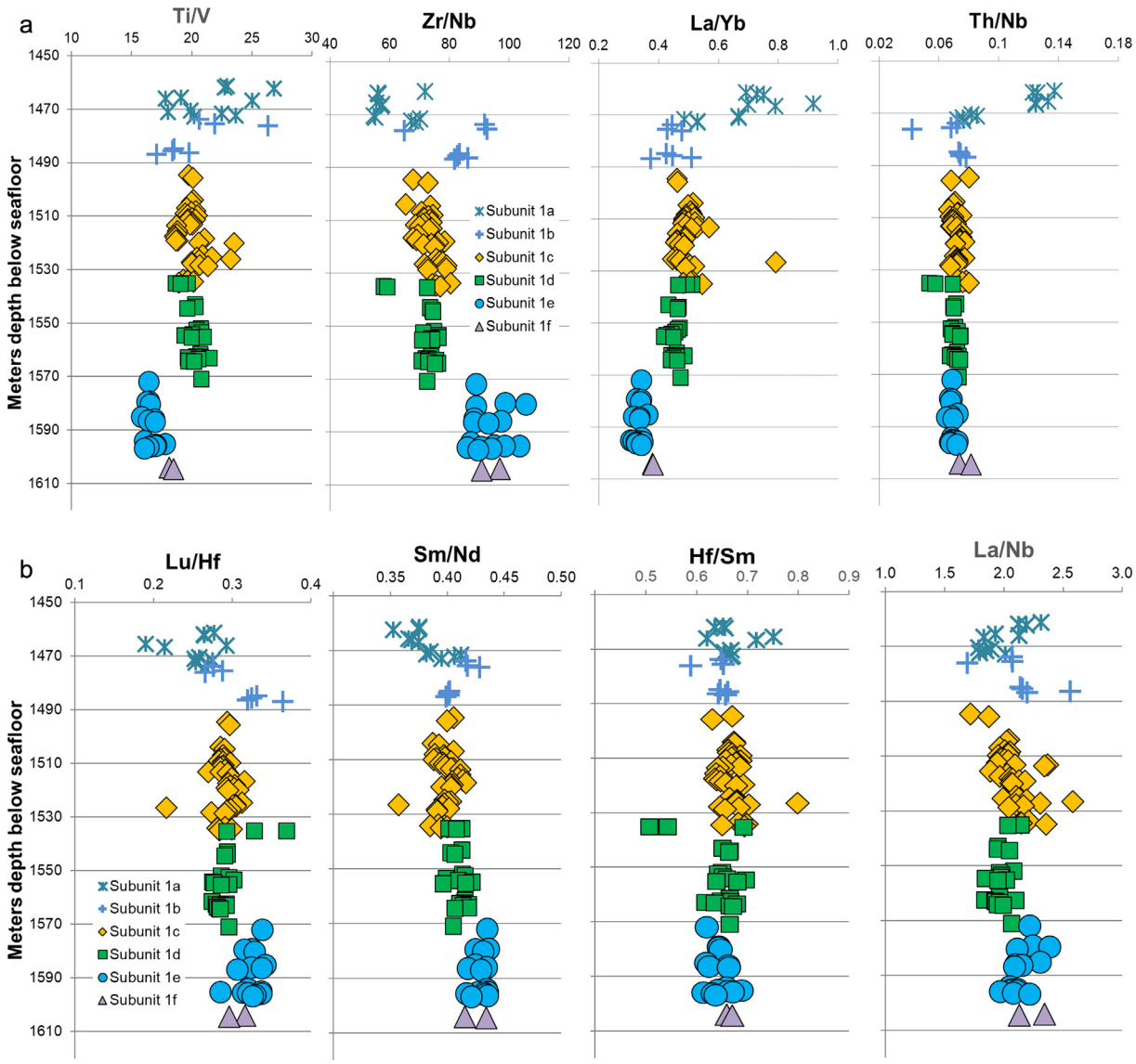

Fig. 7. Down-core variation of (a) Ti/V, Zr/Nb, La/Yb, Th/Nb, and (b) Lu/Hf, Sm/Nd, Hf/Sm and La/Nb in Unit 1 basalts. Data are from Table 1.

interpretation is consistent with lithologic interpretations, and the dominance of phenocryst-poor, aphyric and diabasic igneous textures.

In contrast, some immobile incompatible elements vary significantly in concentration within subunits, without corresponding changes in elemental ratios. This is particularly true of massive subunit 1c, which has a range of about 1.4–1.5 times in Zr, Hf, Ti and other immobile incompatible element concentrations (Fig. 10b and c). These variations correlate only weakly with major element variations within subunit 1c, e.g., Zr, Hf, Ti and REE increase with Fe_2O_3 and decrease with Al_2O_3. This suggests that some compaction and local differentiation may have occurred during solidification, either within the underlying magma feeder system or within thick flows during cooling.

5.1.1. Geochemical effects of alteration by seawater and chemical exchange

One striking feature of Unit 1 is the variation of fluid mobile element concentrations (Rb, K, U) with the subunits defined by lithology and major and compatible element geochemistry (Figs. 6 and 9). Understanding fluid-mobile elements in these potentially subduction initiation-related basalts is critical because they could be an igneous feature, introduced into primary magmas by slab-derived hydrous fluids, or they could be introduced from seawater or hydrothermal fluids subsequent to eruption of lava flows. Enrichments in these elements compared with REE and HFSE is a hallmark of island arc magmas globally (e.g., Gill, 1981; Stern, 2002; Elliott and Eiler, 2003). In FAB from the IBM forearc, slight to moderate enrichment in

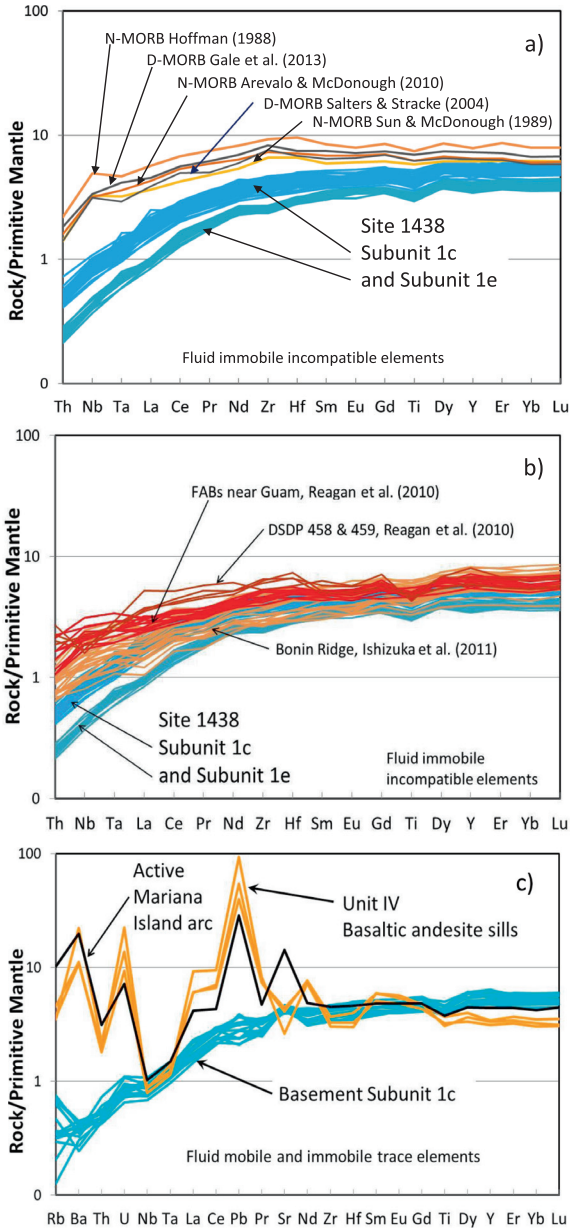

Fig. 8. Normalized abundances of incompatible elements in volcanic rocks from Site U1438. (a) and (b) show fluid immobile trace elements in Unit 1 basalts compared with various types of MORB (a) and FAB (b). N-MORB are from Hofmann (1988), Sun and McDonough (1989), Arevalo and McDonough (2010) and D-MORB are from Salters and Stracke (2004) and Gale et al. (2013). FAB data are from Reagan et al. (2010) and Ishizuka et al. (2011a). (c) shows normalized abundances of both fluid mobile and immobile incompatible elements in andesites in sedimentary Unit IV compared with basalts from basement subunit 1c and the active Mariana Island arc (Elliott et al., 1997).

these elements has been reported, attributed in some cases to slab fluids (Godard et al., 2015) and in others to alteration by seawater or both (Reagan et al., 2010; Pearce et al., 2015; Reagan et al., 2015).

We considered three hypotheses for the origin of the variation in fluid mobile element enrichments: (1) it was a feature of primary magmas and reflected different amounts of slab-derived fluids as a trigger for melting for each subunit; (2) it was a feature of the individual magma batches forming the subunits, introduced by assimilation of hydrothermally altered oceanic crust in the magma feeder system; (3) it was produced by seawater-rock interaction with cooling basaltic flows, with rock physical properties and time controlling the extent of alteration. Our conclusion is the third hypothesis is most likely, and that the down-core fluid mobile element variation is an artifact of syn- and post-eruptive alteration and not a primary feature. In this scenario, subunits 1a, b and d are most affected, and subunits 1c and the lower part of 1e are least impacted by seawater or hydrothermal fluids. Units 1a and b consist of multiple thin flows and have systematically higher LOI (5–11%) than subunits 1c through 1f (Ishizuka et al., 2018). Subunit 1c consists of several 2–5 m, massive, uniformly fine-grained sections. Although the rocks are veined, alteration fronts do not extend far into the rock, suggesting relative impermeability to fluid migration. Unit 1d consists of thin lava flows, which together with this feature in subunits 1a and b, suggests that fluid interaction along flow boundaries was the main pathway for alteration. Subunit 1e consists of thin flows in its upper 20 m near its contact with subunit 1d, and fluid mobile elements are variable, whereas fluid mobile element concentrations diminish in the lower 2 m (Fig. 9). Evidence against a connection with the original magma composition of different subunits, either by introduction of subduction fluids or assimilation of altered basalt, is: (1) the wide variation of fluid mobile element abundances between successive lava flows within subunits 1a, b and d (Figs. 6 and 9); and (2) the lack of subunit specific values for fluid mobile element ratios, e.g., Rb/Ba, K/U (Fig. 9), which indicates independent behavior of each element. Assimilation of altered rock would also be expected to correlate with major element and mineralogical features of the basalts, and this is not observed. Therefore, our interpretation is that enrichment in fluid mobile trace elements resulted from hydrothermal alteration, which was enhanced by the permeability of the different rock subunits and possibly the time over which each flow and subunit cooled on the seafloor. This conclusion could be tested using the compositions of fresh melt inclusions in phenocrysts, but these have not been found to date.

5.1.2. Geochemical changes in uppermost subunit 1a

In addition to the alternating increase and decrease of fluid mobile element concentrations in the differing subunits down-core, the uppermost 12 m of Unit 1 shows some unique features: MgO contents reach 13.8%, SiO_2 increases to 56.6% while other major element contents (e.g., TiO_2, Fe_2O_3, CaO) decrease, and Na_2O/CaO reaches 0.8. Th contents increase to 0.1 ppm from a down-core average of 0.04 ppm, and La/Sm and La/Yb increase slightly (Fig. 11). The major element changes in subunit 1a are common effects of hydrothermal alteration on ocean floor basalt. During exchange with seawater, MgO, H_2O and SiO_2 are added to basaltic crust, forming clays, chlorite and silica, whereas Na_2O and H_2O are added through albitization and zeolitization of feldspar (Alt et al., 1986; Alt and Teagle, 2003).

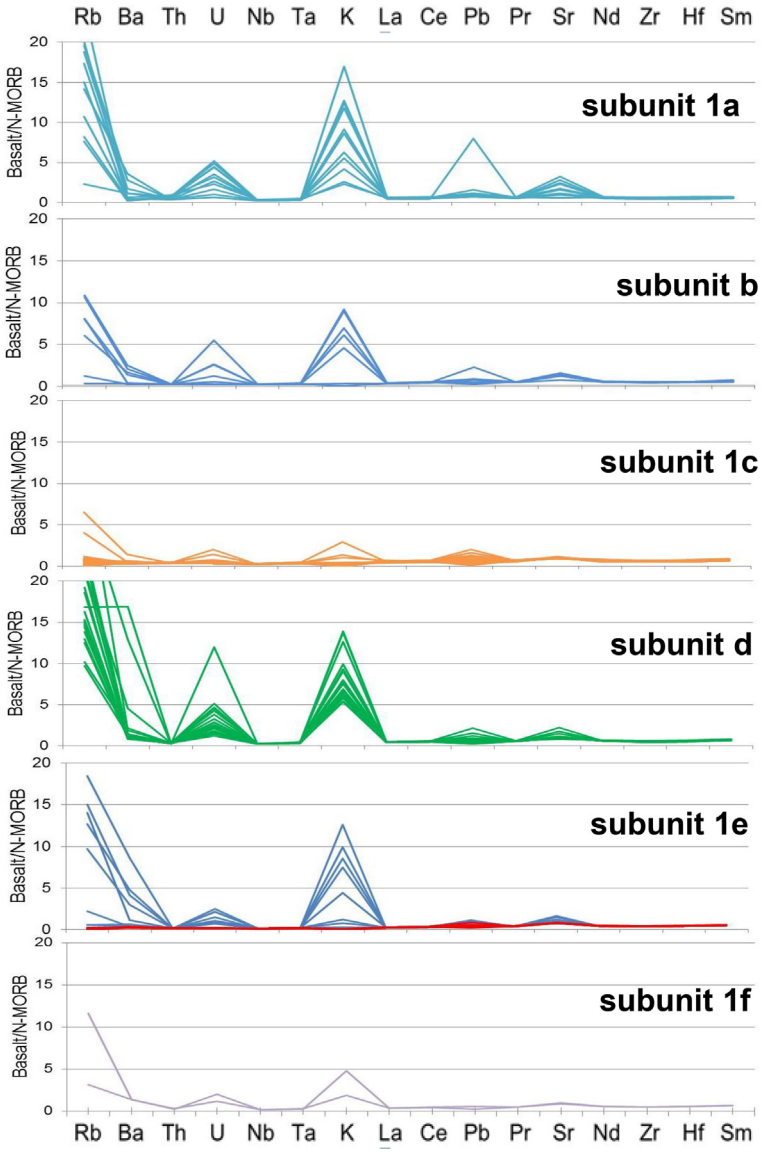

Fig. 9. Variation in abundances of fluid mobile elements Rb, Ba, U, K, Pb and Sr within and between Unit 1 subunits. Abundances are normalized to N-MORB (Sun and McDonough, 1989). Adjacent fluid-immobile element abundances are shown for comparison. Samples shown in red for subunit 1e are from the lower section of this unit.

The extreme MgO contents and Mg#'s in subunit 1a diverge from the overall correlation of Mg# with Cr content in Unit 1 basalt (Fig. 10a). Using Cr content as a guide, the original MgO contents of subunit 1a may have been slightly higher than subunit 1e, near 9–10% MgO, with similar Mg#s to subunit 1e. Together, the pattern of major and fluid mobile element change in the basalts suggests pervasive exchange with seawater, controlled in part by the permeability of the cooling subunits, followed by prolonged exchange of the uppermost surface of the basaltic basement as volcanism waned. The region of scattered elemental abundances at the contact of subunits 1c and 1d could indicate another episode of more prolonged cooling and exchange.

Decreases in abundances of Ti and V, coupled with increases in Th, Nb, Ta and LREE in upper subunit 1a are puzzling because they involve elements that are normally considered immobile in fluids (Johnson and Plank, 1999; Elliott and Eiler, 2003). To some extent, decreases in element abundances may result from dilution caused by precipitation of excess Mg and Si, in addition to their removal in hydrothermal solutions. A possible source for excess Th and LREE may be the overlying sediment. Dark colored, clay and metal-rich "umber" is found from the basalt-sediment contact to 1 m above within sedimentary Unit IV (Fig. 2). Chemical analyses of these sediments show that they have Th, Nb, Ta and LREE contents several times higher than those in the basalts (Fig. 11; Supplementary

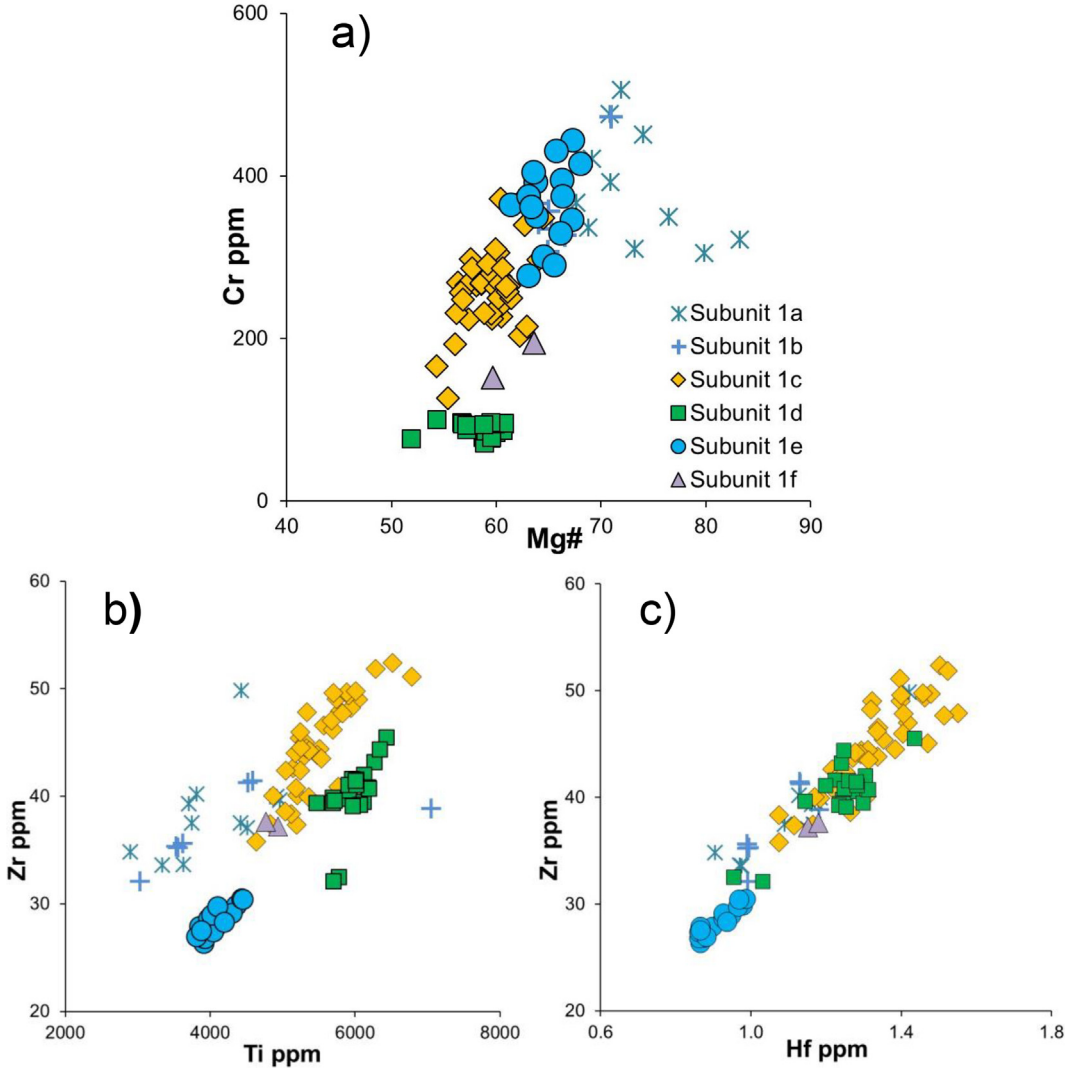

Fig. 10. Trace element variations related to magmatic differentiation. (a) Correlation of Cr with Mg# in different Unit 1 basalt subunits; (b and c) variation of Zr versus Ti and Hf within Unit 1 basalt subunits.

Table 2). Chemical interaction of basalt and sediment could take place in a variety of ways, but the pattern of enrichment focused at the sediment interface suggests that reactions between circulating hydrothermal fluids and basalt resulted in elemental exchange with the metalliferous sediments as they accumulated. The origin of such sediments is widely held to be volcanic exhalative or hydrothermal (e.g., Mills et al., 1993; Mills and Elderfield, 1995), so it is probable that hydrothermal activity, possibly driven by volcanism nearby, continued after basalts ceased to be erupted at the location of Site U1438.

It is important to note that geochemical changes in upper subunit 1a do not match the transition to Si-rich FABS and boninites noted at the forearc locations of IODP Expedition 352 (Reagan et al., 2017). Si-rich FABs and boninites do not have high Na_2O/CaO, and LREE enrichment is more pronounced than what is seen in subunit 1a samples. Although Ti and V contents are lower, Ti/V ratios increase in subunit 1a, opposite the trend noted in FAB and boninites. Th/La ratios are lower than in boninite, while Hf/Sm ratios, which are typically high in boninite (e.g., Crawford et al., 1989), are not elevated (Fig. 7b). Most importantly, Nd and Hf isotopes are not less radiogenic at the top of the basement section in subunit 1a in comparison to the underlying subunits 1b-1f (Yogodzinski et al., this volume). Although lower Nd and Hf isotope ratios might be expected as the result of hydrothermal alteration, samples for isotopic analysis were leached intensely prior to analysis, while samples analyzed for major and trace element analysis were not leached, but were selected to be representative and least altered, but not necessarily unaltered. Our conclusion is that most changes in upper subunit 1a reflect alteration and that the original composition of subunit 1a may have been similar to subunit 1b and subunit 1e. Further investigation using trace element analysis of fresh minerals and melt inclusions may resolve this issue.

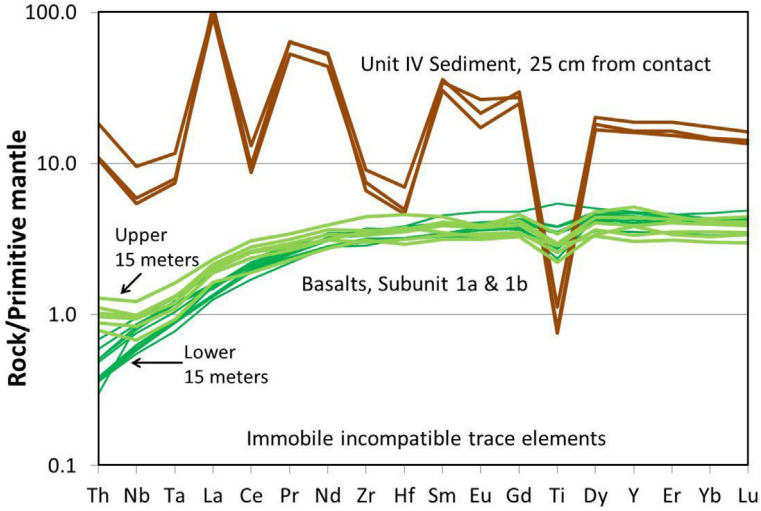

Fig. 11. Normalized abundances of trace elements in metalliferous sediments overlying Unit 1 compared with subunit 1a and 1b basalts. Data for Unit IV sediments are in Supplementary Table 2.

5.2. Comparison of basalts with MORB and FAB

5.2.1. Ti-V-Sc relationships

Exploration of the present-day Mariana and Izu-Bonin islands and submarine exploration of the IBM forearc led to the conclusion that the sequence of magma types produced during subduction initiation is FAB, followed by and to some extent concurrent with boninite, followed by more typical island arc rocks such as low-K tholeiites and calc-alkaline rocks. IBM FAB are tholeiitic basalts with flat to LREE-depleted signatures, similar to MORB, but with some differences that vary from location to location (Reagan et al., 2010; Ishizuka et al., 2011a). The definitive geochemical feature distinguishing FAB from MORB proposed by Reagan et al. (2010) is high V concentrations relative to Ti in FAB, yielding lower Ti/V, typically 10 to 15. As shown in Fig. 12a, recently sampled FABs from IODP Expedition 352 drill sites exhibit this feature. Low Ti/V has been used to fingerprint FAB in studies of arc basement rocks and in ophiolites (Stern et al., 2012; Ishizuka et al., 2014). Reagan et al. (2010) proposed two causes of the low Ti/V in FABs: oxidation and enrichment of V during melting, and mantle depletion in Ti. The first scenario follows the reasoning of Shervais (1982), that island arc basalts have lower Ti/V compared with basalts from mid-ocean ridge and mantle plume environments as the result of source oxidation by slab-derived hydrous fluids. Oxidizing conditions result in higher V concentrations during melting, as moderately incompatible V^{+3} is oxidized to highly incompatible V^{+5} decreasing its partition coefficients (K_ds) for pyroxene. This behavior has been confirmed experimentally and the relationship between V partitioning and varying conditions of oxygen fugacity has been calibrated (Canil, 1999; Mallman and O'Neill, 2009). Using Fe speciation studies, Brounce et al. (2015) have further confirmed that more oxidizing conditions exist in subduction zones compared with MORB mantle sources, commencing during subduction initiation. In an early subduction initiation setting, close to the plate edge, oxidizing conditions may prevail, especially if introduction of hydrous fluids from the slab has begun, leading to the high V and low Ti/V of FABs.

Basalts from Site U1438 have Ti/V from 16 to 27, with highest and most variable values in altered subunit 1a. If these values are excluded, Ti/V ratios vary down-core, with lowest ratios in subunit 1e (Fig. 12a). Since Ti/V ratios in the Site U1438 subunits vary from MORB-like to FAB-like at a single location, we can better constrain how mantle melting conditions versus mantle source depletion influence this ratio. Unlike FABs, Site U1438 basalts show a pattern of decreasing Ti/V with decreasing Ti and V concentrations (Fig. 12a), with subunit 1e approaching Ti/V of average DMM and both Ti and V concentrations at the extreme low end of the MORB field. Fig. 12b shows V concentrations compared with Sc, a trace element similar in behavior to V^{+3} in peridotite minerals, but which only occurs as Sc^{+3} in the solid Earth (Mallman and O'Neill, 2009). In peridotites, Ti, V and Sc are largely hosted in pyroxenes, with partition coefficients increasing from Ti to V to Sc, and with lower K_ds for V under more oxidizing conditions (Mallman and O'Neill, 2009). In Fig. 12b, Sc and V contents for FABs and MORBs overlap, with somewhat higher V for a given Sc in FABs. In contrast, Site U1438 basalts have Sc contents overlapping the MORB field, with V/Sc ratios and V contents decreasing toward subunit 1e. Overall, these relationships suggest that mantle oxidation for Site U1438 basalt and MORB melting was similar, while FAB sources may have experienced enhanced V incompatibility during partial melting, producing an offset toward high V. During mantle melting, Sc is retained in peridotite minerals relative to Ti and V, so partial melts will have higher Ti/Sc and V/Sc than their sources. That Site U1438 basalts have lower Ti/Sc and V/Sc than most MORB, approaching values for DMM in depleted subunit 1e, indicates that their mantle sources were originally depleted in Ti and V, and that their low Ti/V ratios result in part from that original depletion in addition to the mantle melting that generated them at 49 Ma.

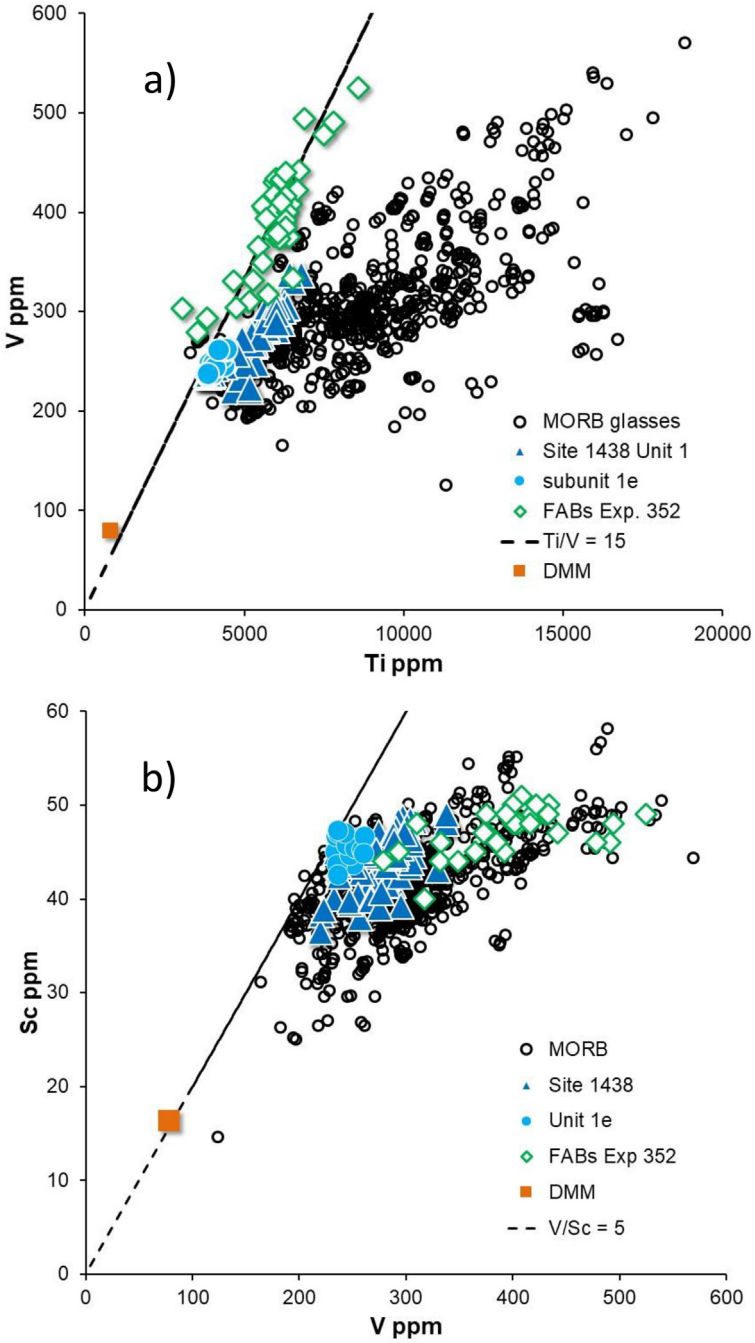

Fig. 12. Plots of V versus Ti and Sc versus V for different Unit 1 subunits, MORBs (Jenner and O'Neill, 2012) and FABs from IODP Expedition 352 sites in the Izu-Bonin forearc (Reagan et al., 2017). DMM is depleted MORB mantle of Salters and Stracke (2004).

5.2.2. Depletion of immobile incompatible elements in Site U1438 basalts

Site U1438 basalts exhibit extreme depletion in highly incompatible elements, with ratios such as La/Yb, La/Sm, Nb/Zr, Nb/La and Th/La, and elemental abundances at the lower limits of those found in MORB (Fig. 8a). Some IBM FAB, especially those from the Bonin Ridge, also plot at the depleted extreme of global MORB (Fig. 8b). The low incompatible element abundances in Site U1438 basalts compared with MORB can be produced by a high extent of melting of MORB mantle sources (DMM), or by a lower extent of melting of a previously melted and thus ultra-depleted MORB source (D-DMM, see discussion below). The unusually low highly incompatible/moderately incompatible element ratios in Site U1438 basalts are more consistent with the latter model, under specific conditions: (1) the initial depletion event to form the local D-DMM sources extracted only the most incompatible elements, as would be the case for a small degree of fractional melting, and (2) that the extraction of melt during initial formation

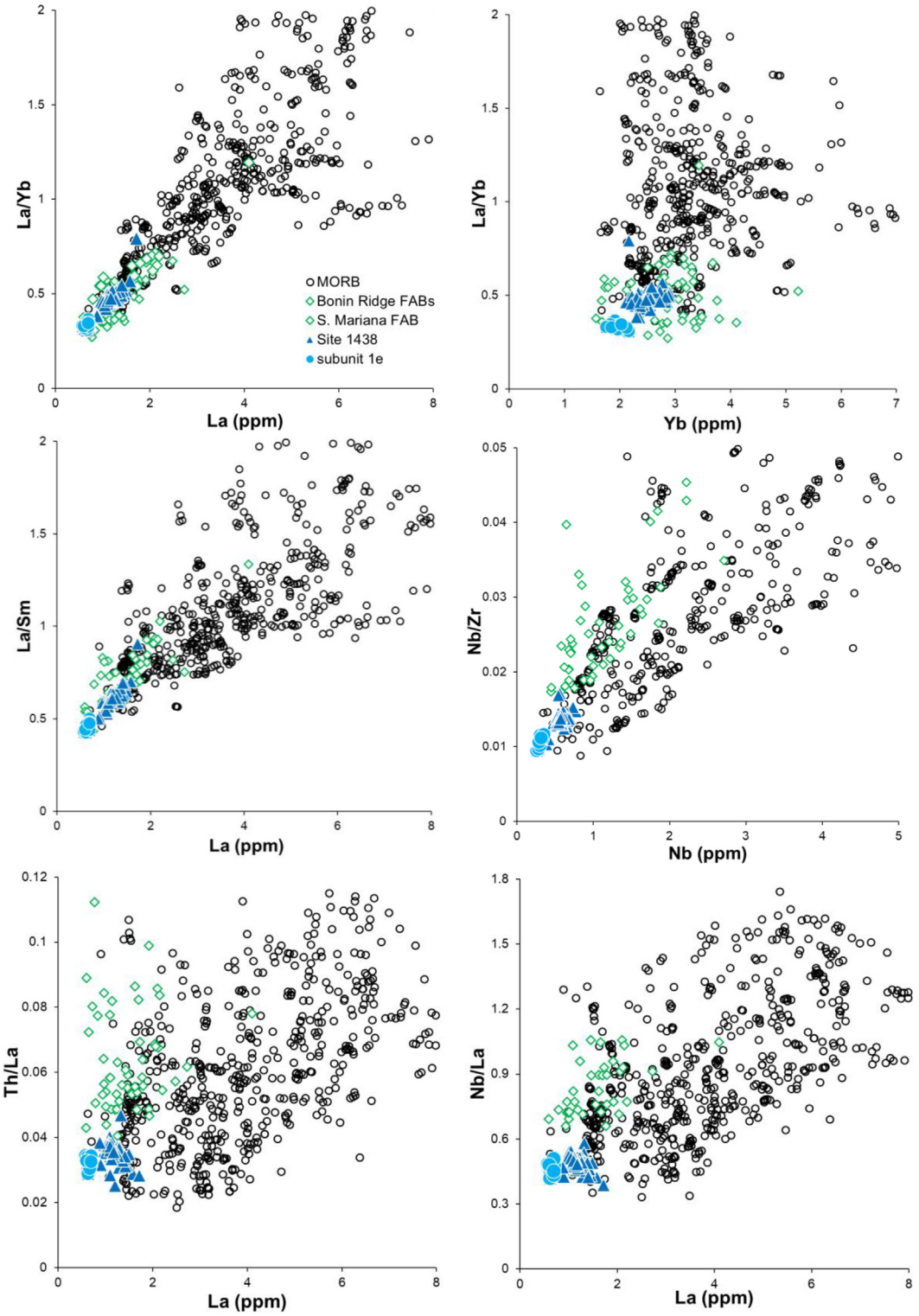

Fig. 13. Ratio – element plots comparing Site U1438 basalts and FABs with MORBs. References are in the caption to Fig. 12.

of the local D-DMM source was exceptionally efficient, with no trapped melt component to increase highly incompatible element abundances from those expected from mineral/melt partitioning (Langmuir et al., 1992). Ongoing research has identified different MORB types and different MORB sources, ranging from depleted to enriched (e.g., Hofmann, 1988; Sun and McDonough, 1989; McDonough and Sun 1995). Salters and Stracke (2004) estimated the composition of depleted MORB (D-MORB; Fig. 8) and D-MORB mantle sources (D-DMM; Fig. 14).

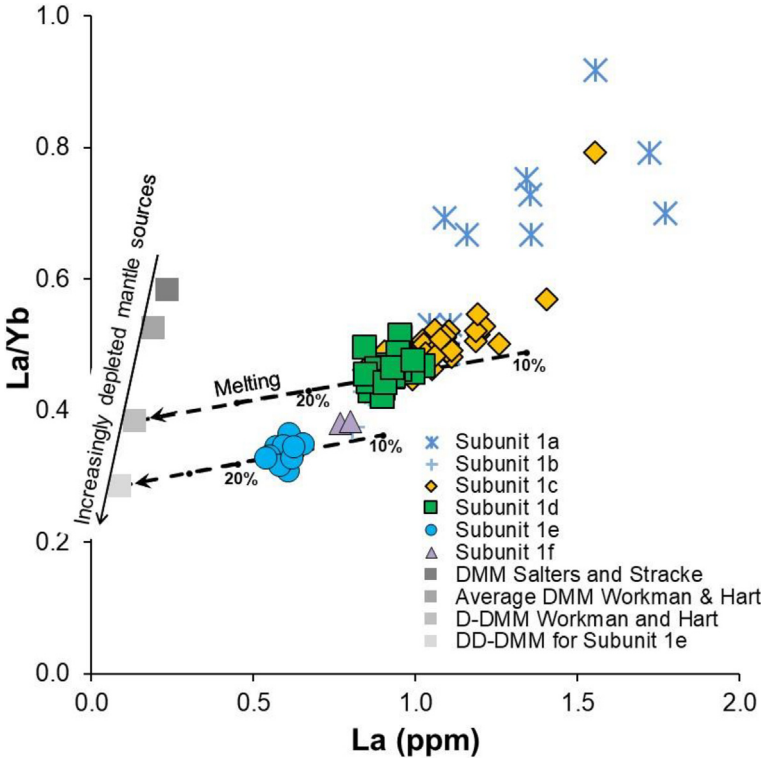

Fig. 14. Plot of La/Yb vs La showing a model for melting of variably depleted mantle sources to form Site U1438 primary basalts (Supplementary Table 3). Increasingly depleted mantle sources are: DMM (Depleted MORB mantle) of Salters and Stracke (2004); average DMM of Workman and Hart (2005); depleted DMM or D-DMM of Workman and Hart (2005) and DD-DMM inferred for subunit 1e basalts.

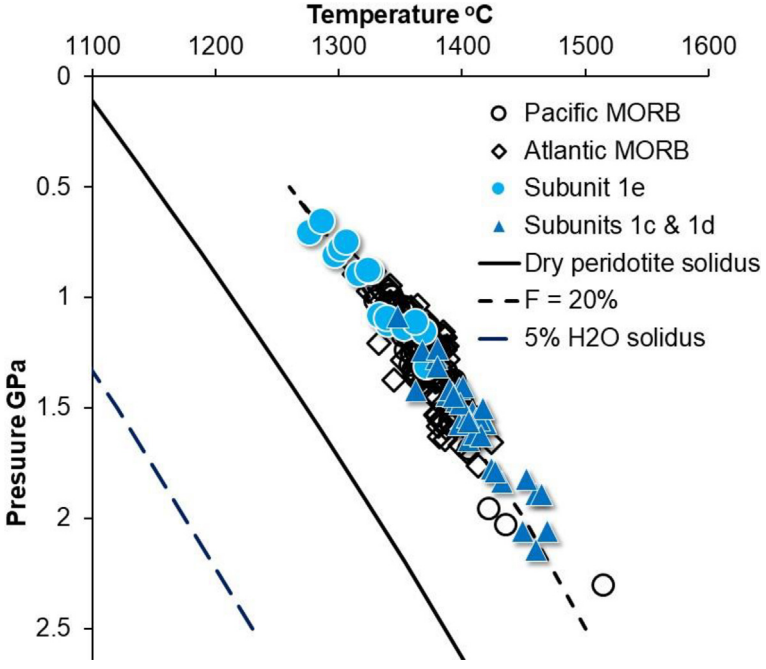

Fig. 15. Temperature and pressures of melt extraction for Site U1438 primary basalts compared with MORB. Samples with MgO > 8% are recalculated for equilibrium with Fo_{90} olivine using the algorithm of Lee et al. (2009) (Supplementary Table 3). The dry peridotite solidus, 20% melting isopleth and hydrous solidus with 5% H_2O from Katz et al. (2003) are shown for comparison.

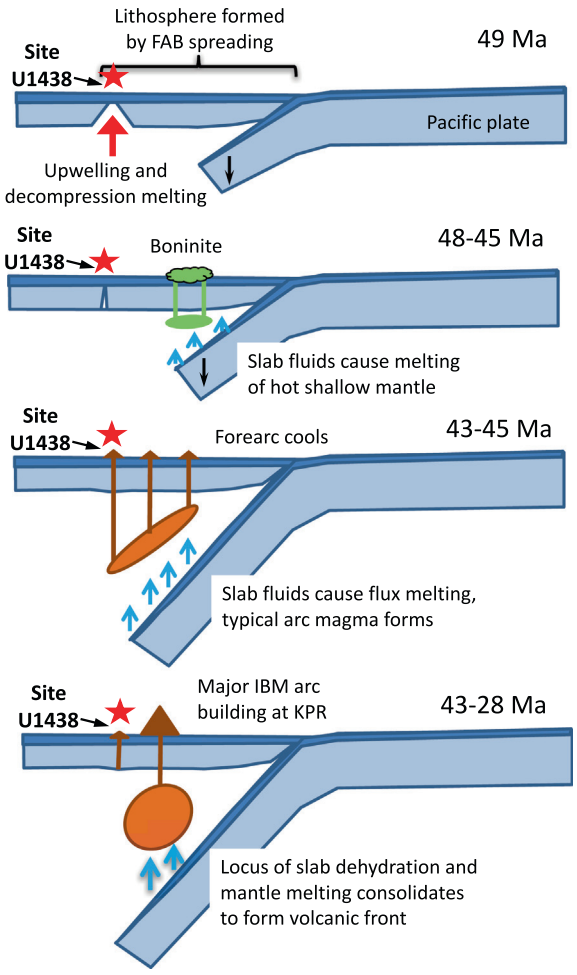

Fig. 16. Cartoon showing a scenario for the origin of Site U1438 volcanic rocks in the context of subduction initiation and early arc development in the IBM system. See text for explanation.

Workman and Hart (2005) modeled DMM using analyses of abyssal peridotites, and conclude that primary N-MORB is generated by 6% aggregated fractional melting. They define average, depleted (D-DMM) and enriched DMM sources, and estimate that the average N-MORB source formed by 2–3% melt extraction from the primitive mantle (Fig. 14). Arevalo and McDonough (2010) calculate a global MORB average and N-MORB, and compile regional differences in trace element ratios (Fig. 8). Gale et al. (2013) define N-MORB, D-MORB and E-MORB types based on a database of worldwide MORB analyses (Fig. 13).

In Fig. 13, highly incompatible/less incompatible element ratios La/Yb, La/Sm, Nb/Zr Th/La and Nb/La are plotted versus abundance, showing data for Site U1438 basalts, MORB from the databases of Jenner and O'Neill (2012) and Gale et al. (2013) and IBM FAB (Reagan et al., 2010, Ishizuka et al., 2011a; Reagan et al., 2013). In each case, the Site U1438 basalts plot at the extreme low ratio-low abundance ends of MORB fields, with subunit 1e showing the most extreme depletion. Given that elements La, Nb and Th have bulk partition coefficients approaching 0 for peridotite melting, it is likely that differences in these ratios from MORB and among the different subunits arise from variations among previously depleted mantle sources, rather than fractionation during melting to form basaltic magma. The concept that their sources originally had differing ratios of highly incompatible to moderately incompatible elements is borne out by correlations between parent/daughter element and isotope ratios in the Lu-Hf and Sm-Nd systems (Yogodzinski et al., this volume). These correlations point to a mantle depletion episode prior to remelting during subduction initiation. Trace element abundances, on the other hand, reflect both the extent of source depletion and the extent of melting to form magma.

5.2.3. *Melting model for Site U1438 basalts*

Fig. 14 shows a schematic model for melting of progressively depleted mantle sources to produce primary basalts from subunits 1d and 1e. The sources for these subunits have different La and Yb contents and La/Yb ratios. We used the D-DMM source of Workman and Hart (2005) and La (bulk D = 0) to estimate about 15% partial melting for subunit 1d. This is significantly higher than that estimated by Workman and Hart (2005) for N-MORB. Applying the same melting parameters to subunit 1e yields the low La/Yb and La contents in its source, DD-DMM. Unaltered basalts from subunits 1b, 1c and 1f plot roughly along melting curves defined by subunits 1d and 1e.

We used the Sc abundances for DMM from Salters and Stracke (2004), Sc K_d's from Mallman and O'Neill (2009) and concentrations of Sc in primary subunit 1d and 1e magmas to estimate the initial modal mineralogy prior to melting. Using 15% non-modal melting from above, initial bulk Ds for Sc are 0.40–0.42 in the sources for subunits 1e and 1d respectively. Spinel peridotite modes having these bulk Ds are non-unique, however, values of 0.40–0.42 indicate at least 15% clinopyroxene. A clinopyroxene-bearing source accounts for the low, but MORB-like, abundances of moderately incompatible (e.g., Ti, Yb, Figs. 12 and 13) and slightly incompatible (e.g., Sc, V, Fig. 12) elements. The mildly depleted slope of the MREE and HREE (Fig. 8) excludes garnet in the source or residue, supporting a shallow melting process. Therefore, we propose that the depleted sources for the Site U1438 subunits formed by differing small extents of melting, leaving a mantle variably depleted in highly incompatible elements, but still fertile, with clinopyroxene, orthopyroxene, olivine and spinel. Subsequent melting to form the Site U1438 basaltic magmas occurred on the order of 15%, diminishing and possibly exhausting clinopyroxene. The residue of this melting is likely to be harzburgite, and could be a source for boninite or other arc basalts (Parkinson and Pearce, 1998).

5.3. Constraints on mantle melting: hydrous versus anhydrous melting

Given the depleted nature inferred for the sources for Site U1438 basement basalts, an important question is what caused the mantle to remelt. A similar issue exists for FAB from the IBM forearc. Hypotheses for mantle melting

during subduction initiation generally are: (1) hydrous slab-derived fluids lower peridotite melting solidi (Gaetani et al., 2003; Reagan et al., 2010; Ishizuka et al., 2011a); (2) decompression due to mantle upwelling in response to plate subsidence (Hall et al., 2003; Gurnis et al., 2004) and (3) heating and upwelling of depleted upper mantle entrained by a rising plume, i.e., plume-induced subduction (Gerya et al., 2015; Whattam and Stern, 2015).

Evidence for different melting regimes can be examined using temperature-pressure arrays estimated for related primary magmas. In Fig. 15, we compare mantle separation temperatures and pressures for dry primary magma compositions for Site U1438 basalts from relatively unaltered subunits 1c-1e with those for present-day MORB, using the thermobarometric model of Lee et al. (2009). For Subunits 1c-1d, melt extraction pressures and temperatures range from 1.1 to 2.1 GPa and 1350° to 1470 °C respectively, while compositions of most depleted subunit 1e yield lower pressures and temperatures of 0.6–1.3 GPa and temperatures of 1280°–1370 °C. Pressures and temperatures for subunit 1e that match other subunits are obtained when a residue with more magnesian olivine (Fo 92) is used in the model. The shallow depths inferred for all subunits are above the stability range of garnet (50–60 km), which is consistent with the absence of residual garnet indicated by the bulk rock trace element signatures, especially the HREE (Fig. 8). Site U1438 primary basalt compositions coincide with those for Pacific and Atlantic MORB, lying along an anhydrous melting isopleth of 20% melting. The coincidence of MORB and Site U1438 basement in inferred melting temperature and pressure suggests that the origin of the basalts is not especially different from the decompression melting of MORB, and that tectonic forces that lead to upwelling are responsible for melting. In models for subduction initiation (Hall et al., 2003; Gurnis et al., 2004), asthenospheric mantle continues to upwell near the contact of the overriding and subsiding plates until subduction and dewatering of the downgoing plate causes cooling of the forearc mantle wedge. Entrainment of depleted upper mantle at the periphery of a rising plume might have a similar result on melting, but would be expected to originate at greater depths and higher temperatures. That basalts from the most depleted subunit with lowest incompatible element contents are extracted at shallower depths may indicate that mantle sources were vertically stratified, with more depleted mantle at shallower depths. Alternatively, the basalts may have originated at similar depths, with a more refractory residue for subunit 1e.

Water will lower the mantle solidus temperature and cause partial melting at lower temperatures (Gaetani et al., 2003). This is clearly the mechanism that causes the voluminous island arc magmatism that develops once true subduction and dehydration of the slab is underway (e.g., Gill, 1981; Stern, 2002). In the initial stages of plate subsidence, before significant underthrusting, there are more limited ways for hydrous fluids to invade the upper mantle and affect peridotite melting. However, introduction of even small amounts of water could lower the solidus by tens to hundreds of degrees (Grove et al., 2006). For Site U1438 basalts, 1% water shifts melting temperatures downward by about 30 °C over the same range of pressure for anhydrous melting. A slightly hydrous parental magma could be inferred from the mineralogy of the basalts (Arculus et al., 2015b), based on the abundant clinopyroxene in the groundmass and as rare phenocrysts. This differs from the dominant olivine-plagioclase mineralogy of MORB and could result from suppression of plagioclase crystallization by H_2O (Arculus et al., 2015b).

In contrast, trace element evidence for the kinds of hydrous fluids that enrich typical subduction-related magma is lacking in freshest Unit 1 basalts. As discussed in Section 5.1.1, enrichment in fluid-mobile elements is largely the result of post-eruptive alteration, and other trace element hallmarks of arc magmas, such as enrichment in LREE and depletion in Nb, Ta, Hf and Zr, are not evident. A possible explanation is that the fluids that triggered melting were relatively solute-poor, so that their impact on magma chemistry was less important than their impact on melting and resulting basalt mineralogy. The low concentration extreme of a fluid available during subduction initiation would be seawater, driven from the oceanic crust at low pressures and temperatures during plate subsidence. As an example of its geochemical impact, approximately 4% of seawater (Quinby-Hunt and Turekian, 1983) dissolved in a MORB basaltic magma (N-MORB, Edmond et al., 1979; Sun and McDonough, 1989) produces a slight decrease in the abundance of elements such as Rb, Ba, U, K and Na, in addition to all other elements shown in Fig. 8, whereas Cl (not analyzed in this work) increases by a factor of 20. The concentrations of solutes in hydrous fluids are expected to increase with pressure and components of dissolved silicates can increase exponentially over a span of less than a kilobar (Walther and Helgeson, 1979; Adam et al., 2014). Partitioning of elements between hydrous fluids and minerals in the slab and mantle at high pressures can also fractionate elements from one another, as observed in typical volcanic arc rocks (Johnson and Plank, 1999). For the Site U1438 basalts, lacking primary fluid-mobile element enrichments, a plausible scenario is that small amounts of solute-poor hydrous fluids are incorporated into the upwelling depleted mantle at depths much shallower than the 80–150 km slab depths typical of island arc magmatism (van Keken et al., 2011), possibly even within 20 km (0.6 GPa) of the seafloor. For FAB from the IBM forearc, which presumably formed near the plate edge, such shallow fluids could easily be incorporated. However, it is more difficult to envision how slab fluids introduced at the plate edge would be transported through the shallow upper mantle to the location of Site U1438.

5.4. Mantle melting regimes, subduction initiation and early arc evolution

Plate reorganization in the western Pacific at 60–50 Ma led to the onset of subduction of the Pacific plate beneath what is now the Philippine Sea plate (Whittaker et al., 2007; Seton et al., 2015). Hypotheses concerning what drove the onset of plate subsidence range from a rapidly changing force balance related to the subduction of the Izanagi plate and Izanagi-Pacific ridge beneath southeastern

Eurasia (Seton et al., 2015; Arculus et al., 2015b) to the juxtaposition of old oceanic lithosphere and the buoyant island arc lithosphere of the Amami plateau and Daito Ridges to the west of the site of plate subduction (Leng and Gurnis, 2015). Of the various potential causes of melting of depleted mantle in the Amami Sankaku basin, decompression and heating together with a rising plume is the least likely based on geochemical arguments. The existence of plume-related basalts in the West Philippine basin was demonstrated by Hickey-Vargas (1998), who showed that basalts from distinct locations had the same strongly incompatible-element enriched and EM-2 isotopic character. MacPherson and Hall (2003) and Deschamps and Lallemand (2004) proposed that this mantle plume served as a thermal source for melting of the mantle, especially to form boninite erupted at the Bonin Ridge. Later, Ishizuka et al. (2013) established the age progression of Oki Daito plume-related basalts, showing the onset of plume volcanism at 51 Ma in the Minami-Daito Basin, at 36 Ma at the Benham Rise and Oki-Daito ridge, with younger OIB-like products closer to the Central Basin Fault (Fig. 1). Although the oldest of these ages coincides with arc initiation, and there is no evidence for blending of sources or melts from depleted upper mantle and an enriched plume, which would be expected if depleted mantle rose by entrainment. Globally, most plume-ridge interactions exhibit some degree of magma and source mixing (Murton et al., 2002; Herbrich et al., 2016). In contrast, basalts from drill sites along the eastern edge of the West Philippine basin are all highly depleted (see Yogodzinski et al., this volume). Although the presence of the Oki-Daito plume in the western West Philippine basin is clear, its relationship with subduction initiation is not resolved.

Mantle upwelling and decompression are consequences of subduction initiation in geophysical models (Hall et al., 2003; Gurnis et al., 2004), and FAB are generated and erupted in the forearc gap during lithospheric foundering and subsidence (Stern, 2004). In a study of northern IBM forearc crust, Ishizuka et al. (2011a) noted sheeted dykes and proposed that FABs erupted by means of sea-floor spreading. Ishizuka et al. (2018) further proposed that complexities in the structure of the upper plate, such as the presence of the Daito ridges and intervening basins, might result in a complex spreading ridge system, with strongly asymmetric spreading in some segments and numerous ridge jumps. Other researchers have also proposed the development of an upper plate riddled with small spreading ridge segments, either parallel to the plate edge or perpendicular (Taylor and Goodliffe, 2004; Leng and Gurnis, 2015; Lallemand, 2016), during subduction initiation. Either asymmetric spreading or a ridge jump to the west could explain the eruption of FAB-like basalts in the Amami Sankaku basin, further from the plate edge and later in the subduction initiation sequence relative to forearc FABs (Fig. 16, 49 Ma; see also Ishizuka et al., 2018, Fig. 7). Assuming FAB generation and spreading occurred along many ridge segments, boninite might be generated in one location while FAB is generated in another, as subduction fluids of varying amount and composition are added to the upwelling upper mantle by the newly subsiding Pacific plate (Fig. 16, 48–45 Ma). In this scenario, Site U1438 basalts may have been generated largely by decompression melting at a site of mantle upwelling and sea-floor spreading behind the forearc, at a distance of 100–200 km (Arculus et al., 2015b) or up to 300 km from the plate edge (Ishizuka et al., 2018).

As significant plate underthrusting and true subduction develops, conditions shift to those leading to typical arc magmatism by the expulsion of deeply sourced subduction fluids and flux melting of the mantle wedge (Stern, 2002; Ishizuka et al., 2011a). Apparently, during this stage (Fig. 16, 45–43 Ma), about 10 Ma following subduction initiation, a small amount of typical arc magma was erupted at the location of Site U1438, as evidenced by the andesitic sills in Unit IV. Following this event, there is no further evidence for magmatism of any kind at Site U1438, although abundant arc volcaniclastic material and ash layers are present in sediments (Arculus et al., 2015b; Brandl et al., 2017). A possible explanation is that the locus of arc magma generation and eruption consolidated over time in the early IBM arc (<43 Ma) as thermal conditions became uniform, stranding Site U1438 basalts and Unit IV andesites in what became the IBM back-arc (Fig. 16, 43–28 Ma). The depth of fluid expulsion became fixed by pressure-sensitive dehydration reactions in the downgoing plate and the overlying zone of mantle melting developed closer to the plate edge than Site U1438. If this scenario is correct, an implication is that the magmatic products of subduction initiation may be spread over a broader swath parallel to the plate edge than subsequent arc volcanoes, and that some "back-arc" crust may in fact be older than the bulk of the arc crust associated with it.

6. CONCLUSIONS

Basaltic basement drilled at Site U1438 in the Amami Sankaku basin formed concurrently with initiation of subduction along the Izu-Bonin-Mariana arc, and is not preexisting oceanic basement on which the IBM arc was constructed. The basalts were erupted approximately 3 Ma after the initiation of subduction at 52 Ma as defined by the oldest ages of FABs located in the IBM forearc. Site U1438 basalts are chemically similar to IBM FABs, but they differ in having slightly higher Ti/V ratios as the result of lower V contents, and no apparent enrichment in fluid mobile elements. Compared with both FABs and MORBs, Site U1438 basalts have low Ti/Sc, V/Sc, La/Yb, La/Sm, Th/La and high Zr/Nb and La/Nb, and low abundances of incompatible elements. The mantle sources of Site U1438 basalts were depleted in highly incompatible elements compared with depleted MORB mantle sources, most likely due to a melting event before their involvement in a subduction initiation setting. Melting of the depleted sources may have been enhanced by the addition of a small amount of solute-poor hydrous fluid, generated at shallow depths and unlike the solute-laden supercritical melts/fluids normally involved in island arc magmatism.

We conclude that magma generation at Site U1438 occurred under less oxidizing and possibly less hydrous conditions than those for FAB, consistent with a location

100–300 km from the plate edge. Mantle melting was caused mainly by upwelling and decompression in a thin and extended upper plate with disorganized and widely separated spreading ridge segments. FABs and then boninites were erupted closer to the plate edge over the same time interval, as water from the downgoing slab progressively invaded the mantle. As subduction proceeded, thermal conditions in the subducting lithosphere and overlying mantle wedge became more uniform, and a well-defined locus of mantle hydrous flux melting and eruption of typical arc magmas developed, forming the early IBM arc, and stranding Site U1438 in a back-arc location. An implication of this work is that FABs and FAB-like basalts are produced during subduction initiation and plate subsidence, forming a broad zone of new lithosphere along the plate edge. As subduction advances, these early basalts may lie both trenchward and in the backarc of the developing island arc front.

ACKNOWLEDGMENTS

This research was supported by grants from the Consortium for Ocean Leadership to R. Hickey-Vargas and G. Yogodzinski, and collaborative National Science Foundation grants OCE1537861 to R. Hickey-Vargas and OCE-1537135 to G. Yogodzinski and M. Bizimis. O. Ishizuka acknowledges Grant-in-Aid (B) (No. 25287133) for sample preparation, and I.P. Savov acknowledges support from the UK-IODP and NERC NE/M007782/1. The authors thank the International Ocean Discovery Program for this opportunity and gratefully acknowledge the input and efforts of all Expedition 351 shipboard scientists, IODP staff and crew of the JOIDES Resolution. R. Hickey-Vargas thanks Dr. Tatiana Trejos and Dr. Jose Almirall of FIU's Trace Evidence Analysis Facility for use of the ICP-mass spectrometers and for sharing their analytical expertise. Thoughtful reviews of the manuscript by Maryjo Brounce, Julian Pearce and an anonymous reviewer are greatly appreciated.

APPENDIX A. SUPPLEMENTARY MATERIAL

Supplementary data associated with this article can be found, in the online version, at https://doi.org/10.1016/j.gca.2018.03.007.

REFERENCES

Adam J., Locmelis M., Afonso J. C., Rushmer T. and Fiorentini M. L. (2014) The capacity of hydrous fluids to transport and fractionate incompatible elements and metals within the Earth's mantle. *Geochem. Geophys. Geosyst.* - **G3**(15), 2241–2253.

Alt J. C. and Teagle D. A. H. (2003) Hydrothermal alteration of upper oceanic crust formed at a fast-spreading ridge; mineral, chemical, and isotopic evidence from ODP Site 801. *Chem. Geol.* **201**, 191–211.

Alt J. C., Honnorez J., Laverne C. and Emmermann R. (1986) Hydrothermal alteration of a 1-km section through the upper oceanic crust, Deep Sea Drilling Project Hole 504B; mineralogy, chemistry, and evolution of seawater-basalt interactions. *J. Geophys. Res.* **91**(10–10), 335.

Arculus R., Ishizuka O., Bogus K., Drab L., Aljahdali M. H., Bandini A. N., Barth A. P., Brandl P. A., Guerra R. d. M., Gurnis M., Hamada M., Hickey-Vargas R. L., Jiang F., Kanayama K., Kender S., Kusano Y., Li H., Loudin L. C., Maffione M., Marsaglia K. M., McCarthy A., Meffre S., Morris A., Savov I. P., da Silva C. A. S., Tepley F. J.,III, van der Land C., Yogodzinski G. M. and Zhang Z. (2015a) International ocean discovery program expedition 351 preliminary report; Izu-Bonin-Mariana Arc origins; continental crust formation at an intraoceanic arc; foundation, inception, and early evolution; 30 May-30 July 2014. Preliminary Report (International Ocean Discovery Program) 351.

Arculus R. J., Ishizuka O., Bogus K. A., Gurnis M., Hickey-Vargas R., Aljahdali M. H., Bandini-Maeder A. N., Barth A. P., Brandl P. A., Drab L., do Monte Guerra R., Hamada M., Jiang F., Kanayama K., Kender S., Kusano Y., Li H., Loudin L. C., Maffione M., Marsaglia K. M., McCarthy A., Meffre S., Morris A., Neuhaus M., Savov I. P., Sena C., Tepley III F. J., van der Land C., Yogodzinski G. M. and Zhang Z. (2015) A record of spontaneous subduction initiation in the Izu-Bonin-Mariana Arc. *Nat. Geosci.* **8**, 728–733.

Arculus R., Ishizuka O., Bogus K., Drab L., Aljahdali M. H., Bandini-Maeder A. N., Barth A. P., Brandl P. A., do Monte Guerra R., Gurnis M. C., Hamada M., Hickey-Vargas R. L., Jiang F., Kanayama K., Kender S., Kusano Y., Li H., Loudin L. C., Maffione M., Marsaglia K. M., McCarthy A., Meffre S., Morris A., Neuhaus M., Savov I. P., da Silva C. A. S., Tepley F. J.,III, van der Land C., Yogodzinski G. M. and Zhang Z. (2015) Proceedings of the International Ocean Discovery Program; Izu-Bonin-Mariana Arc origins; Expedition 351 of the riserless drilling platform from and to Yokohama, Japan; Site U1438, 30 May-30 July 2014. In Proceedings of the International Ocean Discovery Program 351, variously paginated.

Arevalo, Jr, R. and McDonough W. F. (2010) Chemical variations and regional diversity observed in MORB. *Chem. Geol.* **271**, 70–85.

Brandl P. A., Hamada M., Arculus R. J., Johnson K., Marsaglia K. M., Savov I. P., Ishizuka O. and Li H. (2017) The arc arises; the links between volcanic output, arc evolution and melt composition. *Earth Planet. Sci. Lett.* **461**, 73–84.

Brounce M., Kelley K. A., Cottrell E. and Reagan M. K. (2015) Temporal evolution of mantle wedge oxygen fugacity during subduction initiation. *Geology* **43**, 775–778.

Canil D. (1999) Vanadium partitioning between orthopyroxene, spinel and silicate melt and the redox states of mantle source regions for primary magmas. *Geochim. Cosmochim. Acta* **63**, 557–572.

Crawford A. J., Falloon T. J., and Green D. H. (1989). In Boninites, (Ed., A.J. Crawford) Unwin Hyman, London.

Deschamps A. and Lallemand S. (2004) Geodynamic setting of Izu-Bonin-Mariana boninites. *GSA Spec. Publ.* **219**, 163–185.

Edmond J. M., Measures C., McDuff E., Chan L. H., Collier R. and Grant B. (1979) Ridge crest hydrothermal activity and the balances of the major and minor elements in the ocean; the Galapagos data. *Earth Planet. Sci. Lett.* **46**, 1–18.

Elliott T., Plank T., Zindler A., White W. and Bourdon B. (1997) Element transport from slab to volcanic front at the Mariana arc. *J. Geophys. Res.* **102**, 14991–15019.

Elliott T. and Eiler J. M. (2003) Tracers of the slab. *AGU Geophys. Monograph* **138**, 23–45.

Gaetani G. A., Grove T. L. and Eiler J. M. (2003) Experimental constraints on melt generation in the mantle wedge. *AGU Geophys. Monograph* **138**, 107–134.

Gale A., Dalton C. A., Langmuir C. H., Su Y. and Schilling J. (2013) The mean composition of ocean ridge basalts. *Geochem. Geophys. Geosyst.* **G3**(14), 489–518.

Gerya T. V., Stern R. J., Baes M., Sobolev S. V. and Whattam S. A. (2015) Plate tectonics on the Earth triggered by plume-induced subduction initiation. *Nature* **527**, 221–225.

Gill J. B. (1981) *Orogenic Andesites and Plate Tectonics*. Springer Verlag, Berlin.

Godard M., Ryan J. G., Shervais J. W., Whattam S. A., Sakuyama T., Kirchenbaur M., and Reagan M. K. (2015). Geochemistry of the Bonin forearc volcanic sequence; results from IODP expedition 352. AGU 2015 Fall Meeting, San Francisco, CA, Abstract T41E-2948.

Grove T. L., Chatterjee N., Parman S. W. and Medard E. (2006) The influence of H_2O on mantle wedge melting. *Earth Planet. Sci. Lett.* **249**, 74–89.

Gurnis M., Hall C. and Lavier L. (2004) Evolving force balance during incipient subduction. *Geochem. Geophys. Geosyst. - G3* **5**. https://doi.org/10.1029/2003GC000681.

Hall C. E., Gurnis M., Sdrolias M., Lavier L. L. and Mueller R. D. (2003) Catastrophic initiation of subduction following forced convergence across fracture zones. *Earth Planet. Sci. Lett.* **212**, 15–30.

Herbrich A., Hauff F., Hoernle K., Werner R., Garbe-Schoenberg D. and White S. (2016) A 1.5 ma record of plume-ridge interaction at the western Galapagos spreading center (91 degrees 40'-92 degrees 00'W). *Geochim. Cosmochim. Acta* **185**, 141–159.

Hickey-Vargas R. (2005) Basalt and tonalite from the Amami Plateau, Northern West Philippine Basin: New age and geochemical results and their petrologic and tectonic implications. *Island Arc* **14**, 653–665.

Hickey-Vargas R. (1998) Origin of the Indian Ocean-type isotopic signature in basalts from Philippine Sea plate spreading centers: an assessment of local versus large-scale processes. *J. Geophys. Res.* **103**, 20963–20979.

Higuchi Y., Yanagimoto Y., Hoshi K., Unou S., Akiba F., Tonoike K. and Koda K. (2007) Cenozoic stratigraphy and sedimentation history of the northern Philippine Sea based on multichannel seismic reflection data. *Island Arc* **16**, 374–393.

Hofmann A. W. (1988) Chemical differentiation of the Earth; the relationship between mantle, continental crust, and oceanic crust. *Earth Planet. Sci. Lett.* **90**, 297–314.

Ishizuka O., Tani K., Reagan M. K., Kanayama K., Umino S., Harigane Y., Sakamoto I., Miyajima Y., Yuasa M. and Dunkley D. J. (2011) The timescales of subduction initiation and subsequent evolution of an oceanic island arc. *Earth Planet. Sci. Lett.* **306**, 229–240.

Ishizuka O., Taylor R. N., Yuasa M. and Ohara Y. (2011b) Making and breaking an island arc; a new perspective from the Oligocene Kyushu-Palau Arc, Philippine Sea. *Geochem. Geophys. Geosyst.-G3* **12**, Citation Q05005.

Ishizuka O., Taylor R. N., Ohara Y. and Yuasa M. (2013) Upwelling, rifting, and age-progressive magmatism from the Oki Daito mantle plume. *Geology* **41**, 1011–1014.

Ishizuka O., Tani K. and Reagan M. K. (2014) Izu-Bonin-Mariana forearc crust as a modern ophiolite analogue. *Elements* **10**, 115–120.

Ishizuka O., Hickey-Vargas R., Arculus R. J., Yogodzinski G. M., Savov I. P., Kusano Y., McCarth A., Brandl P. A. and Sudo M. (2018) Age of Izu-Bonin-Mariana arc basement. *Earth Planet. Sci. Lett.* **481**, 80–90. https://doi.org/10.1016/j.epsl.2017.10.023.

Jenner F. E. and O'Neill H. S. C. (2012) Analysis of 60 elements in 616 ocean floor basaltic glasses. *Geochem. Geophys. Geosyst - G3*, 13. https://doi.org/10.1029/2011GC004009.

Johnson M. C. and Plank T. (1999) Dehydration and melting experiments constrain the fate of subducted sediments. *Geochem. Geophys. Geosyst. - G3* **1**, 13,479 words.

Karig D. E. (1971) Structural history of the Mariana island arc system. *GSA Bull.* **82**, 323–344.

Katz R. F., Spiegelman M. and Langmuir C. H. (2003) A new parameterization of hydrous mantle melting. *Geochem. Geophys. Geosyst.*. https://doi.org/10.1029/2002GC000433.

Lallemand S. (2016) Philippine Sea Plate inception, evolution, and consumption with special emphasis on the early stages of Izu-Bonin-Mariana subduction. *Prog. Earth Planet. Sci.* **3**. https://doi.org/10.1186/s40645-016-0085-6.

Langmuir C. H., Klein E. M. and Plank T. (1992) Petrological systematics of mid-ocean ridge basalts; constraints on melt generation beneath ocean ridges. *AGU Geophys. Monograph* **71**, 183–280.

Lee C. A., Luffi P., Plank T., Dalton H. and Leeman W. P. (2009) Constraints on the depths and temperatures of basaltic magma generation on earth and other terrestrial planets using new thermobarometers for mafic magmas. *Earth Planet. Sci. Lett.* **279**, 20–33.

Leng W. and Gurnis M. (2015) Subduction initiation at relic arcs. *Geophys. Res. Lett.* **42**, 7014–7021.

Macpherson C. G. and Hall R. (2003) Tectonic setting of Eocene boninite magmatism in the Izu-Bonin-Mariana forearc. *Earth Planet. Sci. Lett.* **186**, 215–230.

Mallman G. and O'Neill H. St. C. (2009) The crystal/melt partitioning of V during mantle melting as a function of oxygen fugacity as compared with some other elements (Al, P, Ca, Sc, Ti, Cr, Fe, Ga, Y, Zr and Nb). *J. Petrol.* **50**, 1765–1794.

McDonough W. F. and Sun S. S. (1995) The composition of the earth. *Chem. Geol.* **120**, 223–253.

McGuire J. J., and Plank, T., et al. (2017) The SZ4D Initiative: Understanding the Processes that Underlie Subduction Zone Hazards in 4D. Vision Document Submitted to the US National Science Foundation, The IRIS Consortium, 63 pp.

Mills R. A. and Elderfield H. (1995) Hydrothermal activity and the geochemistry of metalliferous sediment. *AGU Geophys. Monograph* **91**, 392–407.

Mills R., Elderfield H., Thomson J., Rona P. A. and Thompson G. A. (1993) A dual origin for the hydrothermal component in a metalliferous sediment core from the Mid-Atlantic Ridge. *J. Geophys. Res.* **98**, 9671–9681.

Murton B. J., Taylor R. N. and Thirlwall M. F. (2002) Plume-ridge interaction; a geochemical perspective from the Reykjanes ridge. *J. Petrol.* **43**, 1987–2012.

Parkinson I. J. and Pearce J. A. (1998) Peridotites from the Izu-Bonin-Mariana forearc (ODP Leg 125); evidence for mantle melting and melt-mantle interaction in a supra-subduction zone setting. *J. Petrol.* **39**, 1577–1618.

Pearce J. A., Reagan M. K., Petronotis K., Morgan S., Almeev R., Avery A. J., Carvallo C., Chapman T., Christeson G. L., Ferre E. C., Godard M., Heaton D. E., Kirchenbaur M., Kurz W., Kutterolf S., Li H., Li Y., Michibayashi K., Nelson W. R., Prytulak J., Python M., Robertson A. H. F., Ryan J. G., Sager W. W., Sakuyama T., Shervais J. W., Shimizu K. and Whattam S. A. (2015) International Ocean Discovery Program Expedition 352 Preliminary Report; Izu-Bonin-Mariana fore arc; testing subduction initiation and ophiolite models by drilling the outer Izu-Bonin-Mariana fore arc; 30 July-29 September 2014. Preliminary Reports (International Ocean Discovery Program) 352.

Quinby-Hunt M. S. and Turekian K. K. (1983) Distribution of elements in sea water. *EOS, Trans. Am. Geophys. Union* **64**, 130–132.

Reagan M. K., Ishizuka O., Stern R. J., Kelley K. A., Ohara Y., Blichert-Toft J., Bloomer S. H., Cash J., Fryer P., Hanan B. B., Hickey-Vargas R., Ishii T., Kimura J., Peate D. W., Rowe M. C. and Woods M. (2010) Forearc basalts and subduction

initiation in the Izu-Bonin-Mariana system. *Geochem. Geophys. Geosyst. - G3* **11**, Citation Q03X12.

Reagan M. K., McClelland W. C., Girard G., Goff K. R., Peate D. W., Ohara Y. and Stern R. J. (2013) The geology of the southern Mariana forearc crust; implications for the scale of Eocene volcanism in the western Pacific. *Earth Planet. Sci. Lett.* **380**, 41–51.

Reagan M. K., Pearce, J.A., Petronotis K., Morgan S., Almeev R., Avery A. J., Carvallo C., Chapman T., Christeson G. L., Ferre E. C., Godard M., Heaton D. E., Kirchenbaur M., Kurz W., Kutterolf S., Li H., Li Y., Michibayashi K., Nelson W. R., Prytulak J., Python M., Robertson A. H. F., Rayan J. G., Sager W. W., Sakuyama T., Shervais J. W., Shimizu K. and Whattam S. A. (2015) Proceedings of the International Ocean Discovery Program; Izu-Bonin-Mariana fore arc; Expedition 352 of the riserless drilling platform, Yokohama, Japan to Keelung, Taiwan; Sites U1439-U1442, 30 July-29 September 2014. Proceedings of the International Ocean Discovery Program 352, variously paginated.

Reagan M. K., Pearce J. A. and Petronotis K., et al. (2017) Subduction initiation and ophiolite crust: new insights from IODP drilling. *Int. Geol. Rev.* **59**, 1–12. https://doi.org/10.1080/00206814.2016.1276482.

Salters V. J. M. and Stracke A. (2004) Composition of the depleted mantle. *Geochem. Geophys. Geosyst*. https://doi.org/10.1029/2003GC000597, G3 51, Q05B07.

Seton M., Flament N., Whittaker J., Mueller R. D., Gurnis M. and Bower D. J. (2015) Ridge subduction sparked reorganization of the Pacific plate-mantle system 60–50 million years ago. *Geophys. Res. Lett.* **42**, 1732–1740.

Shervais J. W. (1982) Ti-V plots and the petrogenesis of modern and ophiolitic lavas. *Earth Planet. Sci. Lett.* **59**, 101–118.

Shiki T., Misawa Y., Konda I. and Nishimura A. (1977) Geology and geohistory of the northwestern Philippine sea, with special reference to the results of the recent Japanese research cruises. *Memoirs of the Faculty of Science. Kyoto University Series of Geology and Mineralogy* **44**, 67–78.

Stern R. J. (2004) Subduction initiation; spontaneous and induced. *Earth Planet. Sci. Lett.* **226**, 275–292.

Stern R. J. (2002) Subduction zones. *Rev. Geophys.* **40**. https://doi.org/10.1029/2001RG000108.

Stern R. J., Fouch M. J., Klemperer S. L. and Eiler J. M. (2001) An overview of the Izu-Bonin-Mariana subduction factory. *AGU Geophys. Monograph* **138**, 175–222.

Stern R. J., Reagan M., Ishizuka O., Ohara Y. and Whattam S. (2012) To understand subduction initiation, study forearc crust; to understand forearc crust, study ophiolites. *Lithosphere* **4**, 469–483.

Sun S. S. and McDonough W. F. (1989) Chemical and isotopic systematics of oceanic basalts; implications for mantle composition and processes. *GSA Spec. Publ.* **42**, 313–345.

Taylor B. and Goodliffe A. M. (2004) The West Philippine Basin and the initiation of subduction, revisited. *Geophys. Res. Lett.* **31**. https://doi.org/10.1029/2004GL020136.

Taylor B., Fujioka K., Janecek T. R., Aitchison J. C., Cisowski S. M., Colella A., Cooper P. A., Dadey K. A., Egeberg P. K., Firth J. V., Gill J. B., Herman Y., Hiscott R. N., Isiminger-Kelso M., Kaiho K., Klaus A., Koyama M., Lapierre H., Lovell M. A., Marsaglia K. M., Nishimura A., Pezard P. A., Rodolfo K. S., Taylor R. N., Tazaki K. and Torssander P. (1992) Rifting and the volcanic-tectonic evolution of the Izu-Bonin-Mariana Arc. *Proceedings of the Ocean Drilling Program, Scientific Results* **126**, 627–651.

van Keken P. E., Hacker B. R., Syracuse E. M. and Abers G. A. (2011) Subduction factory; 4, depth-dependent flux of H (sub 2) O from subducting slabs worldwide. *J. Geophys. Res.* **116**. https://doi.org/10.1029/2010JB007922.

Walther J. V. and Helgeson H. C. (1979) Calculation of the thermodynamic properties of aqueous silica and the solubility of quartz and its polymorphs at high pressures and temperatures. *Am. J. Sci.* **277**, 1315–1351.

Whattam S. A. and Stern R. J. (2015) Late Cretaceous plume-induced subduction initiation along the southern margin of the Caribbean and NW South America; the first documented example with implications for the onset of plate tectonics. *Gondwana Res.* **27**, 38–63.

Whittaker J. M., Mueller R. D., Leitchenkov G., Stagg H., Sdrolias M., Gaina C. and Goncharov A. (2007) Major Australian-Antarctic plate reorganization at Hawaiian-Emperor bend time. *Science* **318**, 83–86.

Workman R. K. and Hart S. R. (2005) Major and trace element composition of the depleted MORB mantle (DMM). *Earth Planet. Sci. Lett.* **231**, 53–72.

Associate editor: Janne Blichert-Toft